

\*Corresponding author.

# Self-Attention as Transport: Limits of Symmetric Spectral Diagnostics

Dominik Dahlem\*

Red Hat AI

ddahlem@redhat.com, Diego Maniloff

Red Hat AI

dmanilof@redhat.com, Mac Misiura

Red Hat AI

mmisiura@redhat.com

June 11, 2026

When a language model processes a hallucinated response, its attention routing tends to fail in one of two shapes: over-concentrating on a narrow set of positions, or spreading so diffusely that relevance is diluted, and the shape of the failure carries diagnostic signal. We study these shapes as a diagnostic characterization, computed from attention matrices under *forced scoring* of benchmark-labeled responses rather than during live generation. A widely used family of spectral methods analyzes the symmetric component of the degree-normalized attention operator, which governs transport *capacity*; we prove that every transpose-invariant spectral diagnostic of this operator is structurally *orientation-blind* (it cannot distinguish an operator from its transpose, and therefore cannot detect information-flow direction), with a converse to the blindness theorem bounding any Lipschitz diagnostic’s transpose sensitivity by the asymmetry coefficient  $G$ .

Pairing this with a closed-form bipartite-Cheeger landscape for canonical causal architectures, we show that uniform causal attention satisfies an  $n$ -independent floor  $\phi \geq 1/5$ , while window attention pierces the floor as  $O(w/n)$ ; failure modes are shape-different, not just value-different. This floor is an idealized-architecture benchmark, not an empirical attractor: the fraction of real attention heads that pierce it is itself an architectural signature. The resulting two-axis diagnostic ( $\phi$  for capacity,  $G$  for direction) yields a falsifiable polarity prediction: bottleneck- and diffuse-dominated benchmarks should exhibit opposite polarity. Under length-controlled evaluation, transport features retain interpretable signal (0.62–0.84 LC-AUROC) across the tested decoder-only, encoder-only, and encoder–decoder models, with polarity reversing as predicted between HaluEval and MedHallu.

Red Hat Research



## 1 Introduction

Large language models hallucinate, and the failures are not all alike. Some samples concentrate attention on a narrow set of positions while ignoring relevant context; others spread attention so thinly that no signal carries. These two routing pathologies look quantitatively similar through standard spectral lenses, yet they are mechanistically opposite. Attention-based diagnosis must distinguish them, and the obstacle is structural rather than a matter of finding a better statistic.

Every attention head in a transformer [Vaswani et al., 2017] defines a bipartite transport operator between queries and keys. Degree-normalising this operator yields a scale-invariant representation  $\mathcal{M}$  whose spectral properties encode how information routes through the network. This paper asks what attention-based diagnostics can and cannot measure as a function of which mathematical object they analyse, not to build a stronger hallucination detector, but to characterise the structural boundary.

We establish a structural boundary on what these diagnostics can resolve. The transport operator decomposes orthogonally under the Hilbert–Schmidt inner product into a symmetric component  $\mathcal{M}_{\text{sym}}$  governing transport *capacity* and an antisymmetric component  $\mathcal{M}_{\text{asym}}$  governing transport *direction*. Every spectral diagnostic depending only on singular values or on the symmetric component is invariant under transpose: structurally *orientation-blind* (Theorem 5). A converse to the blindness theorem bounds the transpose sensitivity of any Lipschitz diagnostic by  $\|\mathcal{M}_{\text{asym}}\|_F$ ; the antisymmetric residual is thus the control parameter certified by the converse bound (Theorem 8). This places a precise limit on what symmetric spectral methods such as LLM-Check [Sriramanan et al., 2024], EigenTrack [Ettori et al., 2025], and LapEigvals [Binkowski et al., 2025] can resolve, regardless of which symmetric statistic they extract.

The symmetric axis nevertheless supports a rich diagnostic. The classical Cheeger inequality provides a two-sided bound relating conductance  $\phi$  to the spectral gap  $1 - \sigma_2$ , yielding a certificate for both failure modes: low conductance indicates a bottleneck; anomalously high conductance indicates diffuse mixing. A degree sufficiency theorem (Theorem 3) formalises when coupling structure contributes beyond degree heterogeneity. The antisymmetric axis is targeted by the asymmetry coefficient  $G$ , the normalised Frobenius distance to the symmetric subspace, the minimal complement that recovers directional information.

A closed-form bipartite-Cheeger landscape anchors what healthy routing looks like architecturally. Uniform causal attention satisfies an  $n$ -independent floor  $\phi \geq 1/5$ , while window attention pierces this floor on balanced cuts as  $O(w/n)$  (Sec. 3). The fraction of empirical heads piercing  $1/5$  becomes a population-level architectural signature distinguishing position-encoding regimes.

Length-robust evaluation is a prerequisite, not a contribution: prior work established that a shared length bias in detector scores and correctness labels skews AUROC rankings [Santilli et al., 2025] and that length heuristics alone can match complex detectors under standard automatic evaluation [Janiak et al., 2025]. Spectral features inherit length dependence through three diagnosable confounding channels; length-controlled AUROC deflates raw scores by up to 0.28 points (Sec. 6).

Under this protocol, transport diagnostics retain interpretable signal: between-dataset polarity variation (bottleneck routing on HaluEval, diffuse routing on MedHallu) reflects regime-dependent failure modes predicted by the two-sided theory (Sec. 7).

We make the following contributions. The spine is threefold: (i) symmetric spectral diagnostics are structurally orientation-blind; (ii) Cheeger conductance supplies a two-sided capacity axis with closed-form architectural benchmarks; and (iii) under length control, the polarity of the transport signal is regime-dependent rather than universal. Concretely:

1. A **transport decomposition** of attention operators into symmetric capacity and antisymmetric direction, with a degree sufficiency theorem (Theorem 3) formalizing when coupling structure contributes beyond degree heterogeneity (Sec. 3).
2. An **orientation blindness theorem** with projection characterization and quantitative converse: any spectral diagnostic depending only on singular values or on the symmetric component is transpose-invariant (Theorem 5), and any transpose-sensitive functional must depend on the antisymmetric component proportionally to  $\|\mathcal{M}_{\text{asym}}\|_F$  (Proposition 8). The most concrete falsifiable consequence is the polarity predic-

tion: conductance should show opposite polarity between bottleneck-dominated and diffuse-dominated failure modes.

3. A closed-form **conductance landscape** for canonical causal architectures:  $\phi(S_t) \geq u(t)/(2+u(t))$  with  $u(t) = H_n - H_t$  for uniform causal attention (Theorem 19), yielding an  $n$ -independent floor  $\phi \geq 1/5$  (Theorem 20); window attention pierces this floor on balanced cuts as  $O(w/n)$  (Theorem 16). Failure modes are shape-different, not just value-different; this is the architectural benchmark against which the empirical population fraction of heads piercing 1/5 distinguishes position-encoding regimes (Sec. 3).
4. An empirical **axis profile**: the symmetric axis (capacity) carries the dominant signal in decoder-only transformers; the antisymmetric axis (direction) is sparse but architecture-dependent, with interpretable exceptions in Flan-T5 cross-attention and Pythia RoPE (Sec. 7).

Features are computed without labeled data; calibrated decision-making requires a modest labeled set to establish polarity and thresholds (Sec. 8). Table 1 is the reader’s map: it ties each headline claim to its supporting result, its empirical evidence, and the scope within which it holds.

## 2 Attention as Transport Operators

This section defines the central mathematical object of the paper: the degree-normalized bipartite transport operator  $\mathcal{M}$ . We model attention heads as degree-normalized bipartite transport operators, a formalization that yields scale-invariant diagnostics. This analysis applies to any row-stochastic transport operator; we specialize to attention matrices. Our use of “transport” is structural rather than literal: unlike Sinkformers [Sander et al., 2022], which replace softmax with Sinkhorn normalization so that attention becomes a doubly stochastic optimal-transport plan, we do not solve an optimal transport problem, but analyze the existing attention mechanism *as* a transport operator whose routing quality can be diagnosed through spectral properties. Erel et al. [2025] likewise read the row-stochastic attention matrix as a discrete-time Markov chain, deriving structural properties of its steady-state distribution; we use the transport operator as the object whose spectral geometry bounds what diagnostics can measure. Fig. 1 previews the full diagnostic pipeline, from the raw attention matrix to the two orthogonal axes and the length-controlled evaluation; the objects it names are defined in the remainder of this section.

**Object vs. estimator.** A critical distinction runs through this paper. The true conductance  $\phi$  is a scale-invariant, NP-hard [Šima and Schaeffer, 2006] graph property of the *raw* bipartite attention graph (the graph  $\mathcal{H}(\mathbf{B})$  defined below). The spectral sweep estimator  $\hat{\phi}$  approximates it from finite attention matrices via the degree-normalized operator  $\mathcal{M}$ , and therefore inherits both finite-size and degree-normalization dependence through the estimation process. Observed length correlations in  $\hat{\phi}$  reflect estimator artifacts, not fundamental length-dependence of conductance itself. We maintain this distinction throughout: theoretical statements (the Cheeger inequality, the closed-form architectural bounds) concern the object  $\phi$  on  $\mathcal{H}(\mathbf{B})$ ; empirical results concern the estimator  $\hat{\phi}$  under length-controlled evaluation.

**Definition 1 (Degree-normalized bipartite operator)** Let  $\mathbf{B} \in \mathbb{R}_{\geq 0}^{n_q \times n_k}$  denote the row-stochastic attention matrix for a head (mask applied; softmax over keys), with degree matrices  $D_Q = \text{diag}(\mathbf{B}\mathbf{1})$  and  $D_K = \text{diag}(\mathbf{B}^\top \mathbf{1})$ . The degree-normalized cross-operator is

$$\mathcal{M} = D_Q^{-1/2} \mathbf{B} D_K^{-1/2}. \quad (1)$$

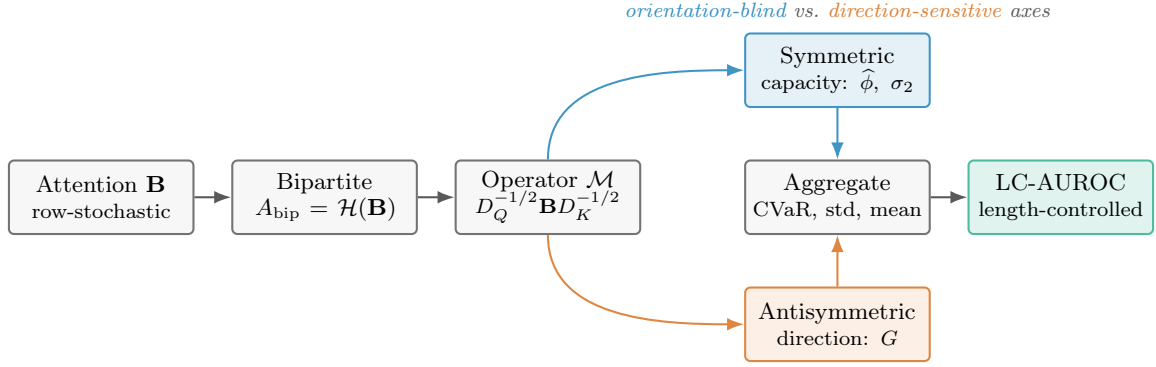


Figure 1: **The transport-diagnostic pipeline.** Each attention head’s row-stochastic matrix  $\mathbf{B}$  is read as a bipartite graph  $A_{\text{bip}} = \mathcal{H}(\mathbf{B})$  and degree-normalized into the operator  $\mathcal{M}$ . The Hilbert–Schmidt-orthogonal split of  $\mathcal{M}$  defines two axes: the *symmetric* component  $\mathcal{M}_{\text{sym}}$  carries transport *capacity*, read by conductance  $\hat{\phi}$  and the second singular value  $\sigma_2$  (every transpose-invariant spectral diagnostic lives here, and is therefore orientation-blind; Theorem 5); the *antisymmetric* component  $\mathcal{M}_{\text{asym}}$  carries *direction*, read by the asymmetry coefficient  $G$  (Theorem 8). Per-axis features are aggregated across layers and heads (CVaR, standard deviation) and evaluated under length-controlled AUROC (Sec. 6.2). Theoretical statements concern the exact object  $\phi$  on  $A_{\text{bip}}$ ; empirical results concern the estimator  $\hat{\phi}$ .

*This operator induces a weighted bipartite graph between queries and keys, and depends only on  $(Q, K)$  and the mask, not on values.*

**Two bipartite graphs.** The symmetric block embedding

$$\mathcal{H}(X) = \begin{pmatrix} 0 & X \\ X^\top & 0 \end{pmatrix} \quad (2)$$

turns a rectangular matrix into a bipartite graph on  $Q \cup K$ . Two such graphs play distinct roles, related by degree normalization. The *raw attention graph*  $A_{\text{bip}} = \mathcal{H}(\mathbf{B})$  carries edge weights  $\mathbf{B}_{ij}$ ; *graph conductance is a property of  $A_{\text{bip}}$* . The *normalized adjacency*  $N_{\text{bip}} = \mathcal{H}(\mathcal{M})$  carries the normalized weights  $\mathcal{M}_{ij}$  and satisfies  $N_{\text{bip}} = D^{-1/2} A_{\text{bip}} D^{-1/2}$ , where  $D$  is the degree matrix of  $A_{\text{bip}}$ . The dilation  $\mathcal{H}(\mathcal{M})$  is symmetric with off-diagonal blocks  $\mathcal{M}$  and  $\mathcal{M}^\top$ , turning the rectangular operator into a symmetric spectral problem whose spectrum is exactly the (signed) singular values of  $\mathcal{M}$ .

**Lemma 2 (Dilation spectrum)** *Let  $\mathcal{M} \in \mathbb{R}^{n_q \times n_k}$  have singular values  $\sigma_1 \geq \dots \geq \sigma_r \geq 0$  with  $r = \min(n_q, n_k)$ . Then  $\mathcal{H}(\mathcal{M})$  has eigenvalues  $\{\pm\sigma_1, \dots, \pm\sigma_r\}$  together with  $|n_q - n_k|$  zeros; consequently the bipartite Laplacian  $\mathcal{L}_{\text{bip}} = I - \mathcal{H}(\mathcal{M})$  has eigenvalues  $1 \pm \sigma_i$ .*

**Sketch.** With the SVD  $\mathcal{M} = U\Sigma V^\top$ , each pair  $(u_i, \pm v_i)/\sqrt{2}$  is an eigenvector of  $\mathcal{H}(\mathcal{M})$ : using  $\mathcal{M}v_i = \sigma_i u_i$  and  $\mathcal{M}^\top u_i = \sigma_i v_i$ ,  $\mathcal{H}(\mathcal{M})(u_i, \pm v_i)^\top = (\pm\sigma_i u_i, \sigma_i v_i)^\top = \pm\sigma_i (u_i, \pm v_i)^\top$ , and the surplus  $|n_q - n_k|$  rows of the larger block span the kernel; see Horn and Johnson [2012], Golub and van Loan [2013].  $\square$

So the SVD of  $\mathcal{M}$  supplies the spectrum of  $N_{\text{bip}} = \mathcal{H}(\mathcal{M})$  at no extra cost. The Cheeger inequality (Sec. 3) bridges these two graphs: conductance on  $A_{\text{bip}}$  to the spectral gap of  $N_{\text{bip}}$ .

With  $\mathcal{M}$  defined as a transport operator, we ask what its spectral structure reveals about routing quality.

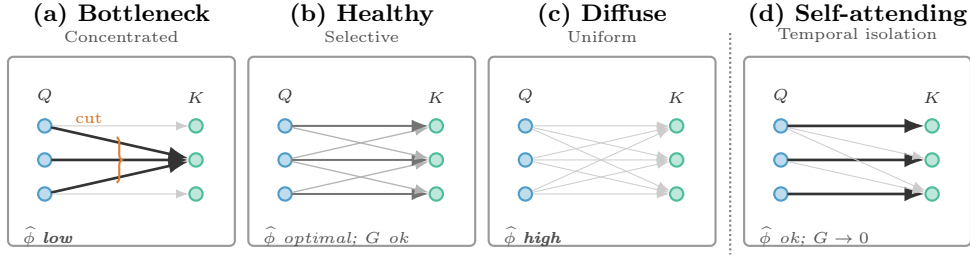


Figure 2: **Conductance has a bounded healthy range; asymmetry detects temporal isolation.** Each attention head defines bipartite transport between queries ( $Q$ ) and keys ( $K$ ). (a)–(c) Conductance spectrum: healthy attention occupies an optimal band; too low indicates bottleneck (a), too high indicates diffuse dilution (c). (a) Bottleneck: concentrated attention yields low  $\hat{\phi}$ , missing relevant context. (b) Healthy: selective routing with task-relevant weighting;  $\hat{\phi}$  in optimal range. (c) Diffuse: uniform attention yields high  $\hat{\phi}$  but dilutes task-relevant signal (Theorem 4). (d) Self-attending (orthogonal axis): as attention concentrates on the diagonal, historical context is ignored;  $\hat{\phi}$  appears normal but  $G \rightarrow 0$ , detectable only by asymmetry coefficient.

### 3 Spectral Structure of Attention

With the transport operator  $\mathcal{M}$  in hand, the natural diagnostic question is: how well does  $\mathcal{M}$  move information between query and key sets? On the raw bipartite attention graph  $A_{\text{bip}} = \mathcal{H}(\mathbf{B})$  this is measured by graph conductance, and the Cheeger inequality bounds that conductance in terms of the spectral gap of the normalized adjacency  $N_{\text{bip}} = \mathcal{H}(\mathcal{M})$ , making the second singular value  $\sigma_2(\mathcal{M})$  a computable proxy for transport quality. This section develops the two diagnostic tools that follow from this framing: conductance and its closed-form architectural benchmark, the spectral gap and a degree-sufficiency theorem that explains when coupling structure contributes beyond degree heterogeneity, and a two-sided diagnostic that certifies both bottleneck and diffuse routing failures.

**Conductance.** Graph conductance is a property of the *raw attention graph*  $A_{\text{bip}} = \mathcal{H}(\mathbf{B})$  (Sec. 2): for a bipartite set  $S \subseteq Q \cup K$ ,

$$\phi(S) = \frac{w(S, \bar{S})}{\min(\text{vol}(S), \text{vol}(\bar{S}))},$$

where the cut weight  $w(S, \bar{S})$  and the volumes  $\text{vol}(\cdot)$  are computed from the edge weights  $\mathbf{B}_{ij}$  of  $A_{\text{bip}}$ . Because  $A_{\text{bip}}$  is symmetric (hence reversible as a Markov chain after volume-normalisation), the classical Cheeger machinery applies even when  $\mathbf{B}$  itself is not doubly-stochastic. Slow mixing means information cannot move efficiently between distant tokens; a bottleneck is any small subset of heads that traps information flow. Low conductance indicates bottlenecked transport (over-concentrated routing).

**The Cheeger inequality.** Cheeger’s original insight was that graph connectivity has a spectral signature. The classical two-sided inequality is the normalized-Laplacian Cheeger bridge: it relates the conductance  $\phi$  of the raw graph  $A_{\text{bip}} = \mathcal{H}(\mathbf{B})$  to the spectral gap  $1 - \sigma_2$  of its normalized adjacency  $N_{\text{bip}} = \mathcal{H}(\mathcal{M})$ , where  $\sigma_2$  is the second singular value of  $\mathcal{M}$  (the eigenvalue–singular value correspondence is Theorem 2):

$$\frac{\phi^2}{2} \leq 1 - \sigma_2 \leq 2\phi. \quad (3)$$

[Cheeger, 1970, Chung, 1997] The lower bound says: if a bottleneck exists (low  $\phi$ ), mixing must be slow (small spectral gap). The upper bound says: if mixing is slow, a bottleneck must exist; this is the *certificate* direction. Together, these bounds justify using  $\phi$  as a diagnostic: spectral structure reveals transport failures, and low conductance certifies over-concentrated routing. The inequality itself is classical; our contribution here is interpretive rather than algebraic. Reading  $\mathcal{H}(\mathcal{M})$  as the relevant graph identifies *which* routing object the symmetric spectrum can certify (and, via orientation blindness, which it cannot), and the closed-form architectural landscape of Theorem 4 turns the existence statement “a bottleneck cut exists” into a per-architecture benchmark.

**Spectral norm variability as transport diagnostic.** The Cheeger inequality (Eq. (3)) directly connects  $\sigma_2$  to conductance:  $\phi^2/2 \leq 1 - \sigma_2 \leq 2\phi$ . When  $\sigma_2$  is close to 1, the spectral gap  $1 - \sigma_2$  is small, and the Cheeger bound guarantees low conductance, a transport bottleneck. Aggregating  $\sigma_2$  standard deviation across layers therefore measures *cross-layer variability in transport capacity*: layers where  $\sigma_2$  fluctuates substantially alternate between tight and loose spectral gaps, indicating unstable routing. The connection above is between the theoretical objects  $\phi$  (the conductance of the raw graph  $A_{\text{bip}}$ ) and  $\sigma_2$ . In practice, exact  $\phi$  is NP-hard to compute, so we work with a spectral-sweep estimator  $\hat{\phi}$ : rank vertices by the second singular vector of  $\mathcal{M}$  (equivalently the second eigenvector of the normalized adjacency  $N_{\text{bip}} = \mathcal{H}(\mathcal{M})$ ) and minimise the sweep conductance over the resulting threshold cuts; details and approximation behaviour appear in Sec. 5. Because the sweep is carried out on the degree-normalized graph  $N_{\text{bip}}$ ,  $\hat{\phi}$  coincides with the object  $\phi$  on  $A_{\text{bip}}$  when the column degrees are near-regular and otherwise differs by a factor controlled by the degree ratio  $\kappa$  (Theorem 3). Like any finite-size estimator,  $\hat{\phi}$  inherits degree and length dependence through the estimation process, which motivates our length-controlled evaluation protocol (Sec. 7).

**Theorem 3 (Degree sufficiency for near-regular attention)** *Let  $A \in \mathbb{R}^{n_q \times n_k}$  be row-stochastic with positive column degrees  $d_j = \sum_i A_{ij}$ . Define  $\mathcal{M} = D_Q^{-1/2} A D_K^{-1/2}$  (with  $D_Q = I$  for row-stochastic  $A$ ),  $\bar{d} = (\sum_j d_j)/n_k$  the mean column degree, and  $\kappa = d_{\max}/d_{\min}$  the degree ratio. Then:*

- (i) **Sharp constraint:**  $\sigma_1(\mathcal{M}) = 1$ .
- (ii) **Spectral perturbation:**  $|\sigma_2(\mathcal{M}) - \sigma_2(A)/\sqrt{\bar{d}}| \leq \max_j |1 - \sqrt{d_j/\bar{d}}| \leq \sqrt{\kappa} - 1$ .
- (iii) **Doubly-stochastic exactness:** When  $A$  is doubly-stochastic ( $\kappa = 1$ ),  $\mathcal{M} = A$  and the bound vanishes.

Part (i) uses only row-stochasticity and positive column degrees:  $\sigma_1(\mathcal{M}) = 1$  holds for *every* such  $A$ , regular or not. The near-regularity parameter  $\kappa$  enters only through the tightness of the perturbation bound in part (ii).

**Proof.** (i) Let  $\sqrt{d_K} \in \mathbb{R}^{n_k}$  denote the vector with entries  $(\sqrt{d_K})_j = \sqrt{d_j}$ . Since  $D_Q = I$ ,

$$(\mathcal{M}\sqrt{d_K})_i = \sum_j A_{ij} d_j^{-1/2} \sqrt{d_j} = \sum_j A_{ij} = 1,$$

so  $\mathcal{M}\sqrt{d_K} = \mathbf{1}$ , and  $\|\sqrt{d_K}\|^2 = \sum_j d_j = \sum_{i,j} A_{ij} = n_q = \|\mathbf{1}\|^2$ ; hence  $\|\mathcal{M}\sqrt{d_K}\| = \|\sqrt{d_K}\|$  and  $\sigma_1(\mathcal{M}) \geq 1$ . Conversely, for any  $x$  set  $y = D_K^{-1/2}x$ ; Cauchy–Schwarz with the row-stochastic weights  $A_{ij}$  gives  $(\mathcal{M}x)_i^2 = (\sum_j A_{ij} y_j)^2 \leq \sum_j A_{ij} y_j^2$ , and summing over  $i$  and swapping the sums,  $\|\mathcal{M}x\|^2 \leq \sum_j d_j y_j^2 = \|x\|^2$ . Hence  $\sigma_1(\mathcal{M}) \leq 1$ , and  $\sigma_1(\mathcal{M}) = 1$ . (ii) Write  $\mathcal{M} - A/\sqrt{\bar{d}} = A\Delta$  where  $\Delta = D_K^{-1/2} - \bar{d}^{-1/2}I$  is diagonal with  $\delta_j = d_j^{-1/2} - \bar{d}^{-1/2}$ . By Weyl’s perturbation theorem,  $|\sigma_2(\mathcal{M}) - \sigma_2(A/\sqrt{\bar{d}})| \leq \sigma_1(A\Delta)$ . Apply Cauchy–Schwarz per

row with row-stochastic weights  $A_{ij}$ :

$$\begin{aligned} \|A\Delta x\|^2 &= \sum_i (\sum_j A_{ij} \delta_j x_j)^2 \leq \sum_i \sum_j A_{ij} \delta_j^2 x_j^2 \\ &= \sum_j \delta_j^2 d_j x_j^2 \leq \max_j (\delta_j^2 d_j) \|x\|^2, \end{aligned}$$

where the first inequality uses  $\sum_j A_{ij} = 1$  and the sum swap uses  $d_j = \sum_i A_{ij}$ . The key cancellation:  $\delta_j^2 \cdot d_j = (1 - \sqrt{d_j/\bar{d}})^2$ , giving  $\sigma_1(A\Delta) \leq \max_j |1 - \sqrt{d_j/\bar{d}}|$ . Since  $d_{\min} \leq \bar{d} \leq d_{\max}$ , each term satisfies  $|1 - \sqrt{d_j/\bar{d}}| \leq \sqrt{\kappa} - 1$  (the case  $d_j \geq \bar{d}$  uses  $d_j/\bar{d} \leq \kappa$ ; the case  $d_j < \bar{d}$  uses  $d_j/\bar{d} \geq 1/\kappa$  and the AM-GM inequality  $1 - 1/\sqrt{\kappa} \leq \sqrt{\kappa} - 1$ ). (iii) For doubly-stochastic  $A$ ,  $D_K = I$  and  $\bar{d} = 1$ , so  $\mathcal{M} = A$  and the bound equals  $\sqrt{1} - 1 = 0$ .  $\square$

This theorem formalizes the near-regular intuition from the degree-preserving null analysis: when degree heterogeneity is moderate ( $\kappa \approx 1$ , equivalently  $\delta$  small for  $\kappa \leq 1 + \delta$ ), the degree normalization is a small perturbation of uniform scaling. The explicit bound  $\sqrt{\kappa} - 1 \leq \delta/2$  for  $\kappa \leq 1 + \delta$  quantifies how much coupling structure contributes beyond degrees, a prediction we test empirically via degree-only baselines, Sinkhorn projection to doubly-stochastic form, and conditional AUROC residualization (Online Supplement, §11).

We hypothesize that factual generation requires accessing specific high-attention tokens (creating degree heterogeneity), while hallucinated generation involves diffuse or inappropriately concentrated attention. The degree sufficiency theorem makes this hypothesis precise: when  $\kappa \approx 1$ , the coupling structure in  $\sigma_2$  is fully accounted for by degrees, and only when  $\kappa$  deviates does coupling structure contribute independently.

**Matched null validation.** A natural objection is that  $\hat{\phi}$  discrimination reflects finite-size estimator artifacts rather than genuine learned structure. Matched null baselines that preserve attention-specific constraints while randomizing learned structure rule this out: hallucination samples deviate systematically from their own null expectations, and z-scoring against the nulls retains discrimination (improving it by 6–8 points on the lower-baseline models; Table 2). Degree-preserving nulls further reveal that  $\hat{\phi}$ 's discriminative power is largely accounted for by the degree distribution (which tokens receive attention) while  $\sigma_2$  retains signal beyond degree heterogeneity.

The Cheeger framework explains this structurally: degree concentration creates low-conductance cuts because high-degree vertices dominate the volume term, so models that hallucinate create characteristic degree distributions that the Cheeger inequality certifies as transport bottlenecks. We report the quantitative decomposition in Sec. 7.

**Two-sided diagnostic.** Unlike metrics that detect only one failure mode, conductance provides diagnostic signal in both directions from a healthy range (Figure 2).

**Theorem 4 (Conductance bounds both failure modes)** *In decoder self-attention ( $n_q = n_k = n$ , causal mask):*

1. **Bottleneck** (*w-window attention*):  $\phi(S_t) \leq w/\min(t, n-t)$  for every nontrivial temporal cut; balanced cuts therefore satisfy  $\phi(S_t) = O(w/n)$ , and late-half cuts satisfy  $\phi(S_t) \leq w/(n-t)$ .
2. **Diffuse** (*uniform causal attention*):  $\phi(S_t) \geq 1/5$  uniformly in  $n$ ; the volume-crossover branch is localised by the formal half-way bound.

*Both patterns indicate failure, and the difference between them is structural: bottleneck attention fails the Cheeger floor on balanced temporal cuts (a global bottleneck family), while diffuse attention has a localised bottleneck candidate flanked by high-conductance regions on both sides. Bottleneck misses context; diffuse dilutes task-relevant signal.*

Low  $\widehat{\phi}$  detects over-concentrated routing (bottleneck); high  $\widehat{\phi}$  detects under-concentrated routing (diffuse attention that dilutes relevance). This two-sided sensitivity distinguishes conductance from prior spectral metrics that detect only one failure mode. The diffuse-side bound is a structural statement: uniform causal attention has conductance bounded away from zero by an  $n$ -independent constant.<sup>1</sup> The claim that diffuse mixing indicates failure is empirical and task-dependent, validated by the tercile analysis in Sec. 7.

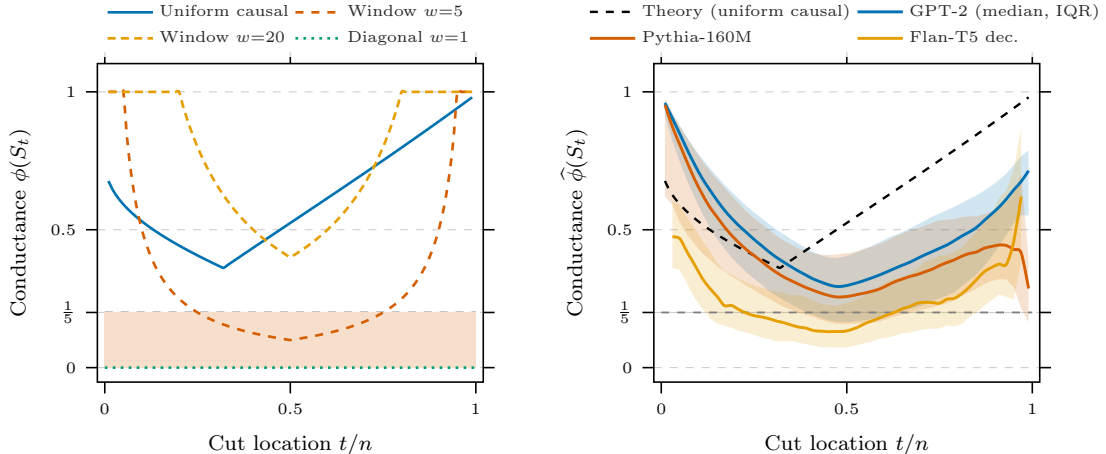
The cut-and-volume identities underlying the diffuse-side bound (Theorem 17, Theorem 18) reveal the *shape* of conductance as a function of cut location:  $\phi(S_t) \geq u(t)/(2+u(t))$  where  $u(t) = H_n - H_t$  is the harmonic mass above  $t$  (Theorem 19). This functional form is the substantive diagnostic content – it tells us where bottleneck candidates sit and how conductance varies smoothly around them, not just that they exist. The same row-sum / column-sum decomposition template applies to any causal architecture (window, exponential decay, RoPE-style decay): each yields its own closed-form cut( $S_t$ ) and vol( $S_t$ ), and the conductance-as-functional-of- $t$  characterises its failure-mode geometry in the same way.

**Empirical landscape signatures.** Real attention does not satisfy the uniform-causal closed form. We compare the closed-form prediction (Fig. 3a) with the empirical landscape from up to 50 HaluEval samples per model (length filter  $n \geq 32$ , exact temporal-cut sweep on the normalized adjacency  $N_{\text{bip}}$ , no Fiedler approximation; median curves with IQR bands in Fig. 3b). The architectural signature lives at the *distribution* level, not at individual heads: the IQR bands of GPT-2 and Pythia-160M overlap substantially across  $t/n$ , so head-by-head separation between these architectures is not supported by the per-cut data. What separates them is the population-level fraction of heads piercing the 1/5 Cheeger floor: 36–42% for GPT-2, 55–70% for Pythia-160M, and 79–82% for Flan-T5 decoder across HaluEval, MedHallu, and TruthfulQA (Table 3, which reports 95% clustered bootstrap CIs). Clustering the bootstrap by sample (the independent unit) widens these intervals well beyond the  $\approx 0.6$  pp a binomial interval over the  $\sim 7200$  correlated (sample, layer, head) rows would give, to as much as  $\pm 4$  pp for the architectures with strongly correlated heads; the architectural ordering GPT-2 < Pythia-160M < Flan-T5 decoder nonetheless remains separated at 95% confidence. The empirical estimator  $\widehat{\phi}(S_t)$  is evaluated on the normalized adjacency  $N_{\text{bip}}$ , whereas the 1/5 value is the floor of the idealized object  $\phi$  on the raw graph  $A_{\text{bip}}$  (Theorem 4); the two graphs differ only by degree normalization (Theorem 3), so the floor is read here as a fixed architectural reference level rather than a literal theorem threshold. Floor-violation fraction is therefore the empirically robust architectural signature; worst-cut location  $t^*/n$  shifts in the same direction (0.50 for GPT-2, 0.51–0.67 for Pythia, 0.48–0.50 for Flan-T5) but with substantial within-architecture variance and overlapping ranges, so it should be read as indicative rather than as a clean architectural classifier.

Proofs can be found in Sec. B.2.3; further details on regime control, masking compatibility, and the Cheeger bridge corollary can be found in Appendix B.

Conductance and  $\sigma_2$  both certify how well the operator  $\mathcal{M}$  *transports* between query and key sets, but neither distinguishes  $\mathcal{M}$  from  $\mathcal{M}^\top$ : they are computed from the symmetric component of  $\mathcal{M}$ . This is a feature for capacity diagnosis and a constraint for direction diagnosis. The next section makes the constraint precise: every spectral diagnostic that depends only on the symmetric component is, by construction, blind to the orientation of routing. That limitation, in turn, identifies the residual structure a directional diagnostic must access.

<sup>1</sup>The constant 1/5 is deliberately conservative: the numerically verified asymptotic floor of the closed-form landscape is  $\approx 0.364$  (checked to  $n = 10^5$ ); we state 1/5 as a clean provable constant.



(a) Theory: failure-mode shapes ( $n = 100$ ). (b) Empirics: HaluEval,  $\leq 50$  samples per model.

**Figure 3: Conductance landscape: theory and empirics.** (a) Theoretical  $\phi(S_t)$  vs. cut location  $t/n$  for canonical causal architectures at  $n = 100$ , derived in closed form from Theorems 16 and 17. Uniform causal (blue, solid) is U-shaped with an  $n$ -independent floor, strictly above the  $1/5$  Cheeger floor (Theorem 20). Window attention (red and orange, dashed) satisfies  $\phi \leq w/\min(t, n-t)$ , hence balanced cuts scale as  $O(w/n)$  and pierce the floor when  $w \ll n$  (shaded red). Diagonal (green, dotted) has exact zero bipartite temporal-cut conductance. Failure modes are *shape-different*, not just value-different. (b) Empirical median  $\hat{\phi}(S_t)$  (solid) with interquartile-range bands (25<sup>th</sup>–75<sup>th</sup> percentile across all (sample, layer, head) tuples) for GPT-2, Pythia-160M, and Flan-T5 decoder on HaluEval ( $\leq 50$  samples per model after the  $n \geq 32$  length filter; exact temporal-cut sweep on the bipartite dilation graph, no Fiedler approximation). Black dashed: closed-form uniform-causal prediction for the object  $\phi$  from panel (a). The IQR bands of GPT-2 and Pythia-160M overlap substantially: head-by-head separation between these architectures is not supported by the per-cut data. What *is* supported is a population-level signature: the fraction of heads piercing the  $1/5$  floor differs sharply (36%, 65%, 79% on HaluEval for GPT-2, Pythia, Flan-T5; binomial  $SE \approx 0.6$  pp at this sample size; Table 3). The closed-form prediction sits below the bulk of every architecture’s IQR for  $t/n \in [0.4, 0.7]$ , confirming the deviation from uniform causal is architecture-wide rather than driven by tail outliers.

## 4 Limits of Symmetric Spectral Diagnostics

Conductance answers “how well does  $\mathcal{M}$  transport?” but says nothing about “in which direction”. This section makes that limitation precise. The underlying algebra is classical: singular values and symmetric spectral embeddings (the Hermitian dilation  $\mathcal{H}(\mathcal{M})$ , the bipartite Laplacian  $I - \mathcal{H}(\mathcal{M})$ , the spectrum of  $\mathcal{M}_{\text{sym}}$ ) are all invariant under  $\mathcal{M} \mapsto \mathcal{M}^\top$ . That Hermitian representations recover directed structure which symmetrization destroys is likewise established for directed-graph clustering by Cucuringu et al. [2020]; we specialize this recovery to attention operators. Our contribution is not a new matrix-analysis fact; it is the identification of what this invariance costs an attention diagnostic, and the precise complement that recovers what is lost.

**Symmetric and antisymmetric components.** For self-attention ( $n_q = n_k = n$ ), any attention matrix admits a canonical decomposition:

$$\mathcal{M} = \underbrace{\frac{1}{2}(\mathcal{M} + \mathcal{M}^\top)}_{\mathcal{M}_{\text{sym}}} + \underbrace{\frac{1}{2}(\mathcal{M} - \mathcal{M}^\top)}_{\mathcal{M}_{\text{asym}}}. \quad (4)$$

Under the Hilbert–Schmidt inner product  $\langle A, B \rangle_F := \text{Tr}(A^\top B)$  Horn and Johnson [2012], this decomposition is an *orthogonal projection*:  $\langle S, A \rangle_F = \text{Tr}(SA) = -\text{Tr}(SA) = 0$  for any symmetric  $S$  and antisymmetric  $A$ . Geometrically,  $\mathcal{M}_{\text{sym}}$  is the closest symmetric matrix to  $\mathcal{M}$ , and  $\mathcal{M}_{\text{asym}}$  captures the antisymmetric residual, the difference  $\mathcal{M} - \mathcal{M}^\top$  that distinguishes the operator from its transpose.

**Why conductance cannot see direction.** Conductance analyzes the symmetric component via spectral properties of the Hermitian dilation. This creates a structural constraint formalized in the following theorem, which combines a transpose-invariance result with its constructive complement.

**Theorem 5 (Orientation blindness of transpose-invariant diagnostics)** *Let  $\mathcal{M} \in \mathbb{R}^{n \times n}$  be a square attention transport operator with symmetric–antisymmetric decomposition  $\mathcal{M} = \mathcal{M}_{\text{sym}} + \mathcal{M}_{\text{asym}}$  (Sec. 2).*

- (a) **Orientation blindness.** *Suppose  $F$  is either (i) a function of the singular values of  $\mathcal{M}$ , or (ii) a function of the spectrum of  $\mathcal{M}_{\text{sym}}$ . Then in both cases  $F(\mathcal{M}) = F(\mathcal{M}^\top)$ , i.e.,  $F$  is transpose-invariant. Moreover, under hypothesis (ii),  $F$  cannot distinguish  $\mathcal{M}$  from any operator sharing the same symmetric part.*
- (b) **Projection characterization.**  *$\mathcal{M}_{\text{sym}}$  is the unique Frobenius-nearest symmetric matrix to  $\mathcal{M}$ , and the residual norm equals  $\|\mathcal{M}_{\text{asym}}\|_F$ . Therefore the pair*

$$\left( \text{symmetric spectral statistic on } \mathcal{M}_{\text{sym}}, G(\mathcal{M}) \right)$$

*decomposes routing structure into the maximal transpose-visible component and the orthogonal residual.*

**Proof structure.**

**Foundations.** The block-swap similarity  $P^\top \mathcal{H}(\mathcal{M}) P = \mathcal{H}(\mathcal{M}^\top)$  for the Hermitian dilation Horn and Johnson [2012]; orthogonality of the symmetric subspace  $\mathcal{S}$  and antisymmetric subspace  $\mathcal{A} = \mathcal{S}^\perp$  under the Hilbert–Schmidt inner product.

**Bridge.** The choice of  $\mathcal{H}(\mathcal{M})$  as the spectral certificate that converts asymmetric  $\mathcal{M}$  into a symmetric eigenvalue problem; the definition  $G(\mathcal{M}, \varepsilon) = \|\mathcal{M}_{\text{asym}}\|_F / (\|\mathcal{M}\|_F + \varepsilon)$  as the antisymmetric-residual control parameter (Sec. 2).

**Contribution.** Every transpose-invariant Lipschitz functional is structurally orientation-blind, and Theorem 8 below tightens this into the quantitative converse  $|F(\mathcal{M}) - F(\mathcal{M}^\top)| \leq 2L\|\mathcal{M}_{\text{asym}}\|_F$ . Together these identify  $G$  as the unique control parameter governing how much transpose-sensitivity any Lipschitz diagnostic can recover, covering spectral entropy, the spectral gap, singular values, graph-Laplacian eigenvalues, and the eigenvalue- and singular-value-based features used in LLM-Check, EigenTrack, and LapEigvals.

**Proof. Part (a).** A concrete certificate of transpose-invariance is the Hermitian dilation  $\mathcal{H}(\mathcal{M}) = \begin{pmatrix} 0 & \mathcal{M} \\ \mathcal{M}^\top & 0 \end{pmatrix}$  (*bridge*). Let  $P$  be the block-swap permutation. Direct block multiplication gives  $P^\top \mathcal{H}(\mathcal{M}) P = \mathcal{H}(\mathcal{M}^\top)$  (*foundations*), so  $\mathcal{H}(\mathcal{M})$  and  $\mathcal{H}(\mathcal{M}^\top)$  are similar and share the same spectrum. Since the singular values of  $\mathcal{M}$  equal the absolute eigenvalues of  $\mathcal{H}(\mathcal{M})$ , any functional of singular values is transpose-invariant. The bipartite Laplacian  $\mathcal{L}_{\text{bip}} = I - \mathcal{H}(\mathcal{M})$  inherits the same invariance (Corollary 7).

**Part (b).** By orthogonality of  $\mathcal{S}$  (symmetric matrices) and  $\mathcal{A}$  (antisymmetric matrices) under the Hilbert–Schmidt inner product (*foundations*),  $\mathcal{M}_{\text{sym}} = \pi_{\mathcal{S}}(\mathcal{M})$  is the orthogonal projection onto  $\mathcal{S}$ . Uniqueness follows from strict convexity of  $\|\cdot\|_F$ . The residual  $\mathcal{M} - \mathcal{M}_{\text{sym}} = \mathcal{M}_{\text{asym}}$  lies in  $\mathcal{A} = \mathcal{S}^\perp$ ; its *orientation* is therefore invisible to any transpose-invariant functional by part (a), such a functional cannot distinguish  $\mathcal{M}_{\text{asym}}$  from  $-\mathcal{M}_{\text{asym}}$ , equivalently  $\mathcal{M}$  from  $\mathcal{M}^\top$  (*contribution*).  $\square$

**Remark 6 (Orientation-blindness vs. asymmetry-blindness)** Part (a) says a symmetric spectral functional cannot distinguish  $\mathcal{M}$  from  $\mathcal{M}^\top$ : it is blind to the orientation of the antisymmetric residual, not to its existence or magnitude. Singular values, for instance, do depend on antisymmetric energy, a purely skew operator has  $\mathcal{M}_{\text{sym}} = 0$  yet nonzero singular values. The asymmetry coefficient  $G$  is itself transpose-invariant,  $G(\mathcal{M}) = G(\mathcal{M}^\top)$ : it quantifies how much asymmetry is present while remaining blind to its sign. What no transpose-invariant functional can recover is which of  $\mathcal{M}, \mathcal{M}^\top$  is the forward operator, the routing polarity.

**Corollary 7 (Blindness of common spectral attention diagnostics)** Any diagnostic computed from the eigenvalues or singular values of  $\mathcal{M}_{\text{sym}}$ ,  $\mathcal{H}(\mathcal{M})$ , or the bipartite Laplacian  $\mathcal{L}_{\text{bip}} = I - \mathcal{H}(\mathcal{M})$  (together with any eigenvector summary invariant under the block swap  $\mathcal{M} \mapsto \mathcal{M}^\top$ ) is invariant under  $\mathcal{M} \mapsto \mathcal{M}^\top$ . This invariant class includes spectral entropy, the spectral gap ( $1 - \sigma_2$ ), graph Laplacian eigenvalues, and the eigenvalue- and singular-value-based features used in LLM-Check, EigenTrack, and LapEigvals.

**Proof.** The SVD singular values equal the absolute eigenvalues of  $\mathcal{H}(\mathcal{M})$ , which are transpose-invariant by Theorem 5(a). The bipartite Laplacian eigenvalues are  $1 \pm \sigma_i$  (Theorem 2), hence also transpose-invariant. Eigenvectors themselves are *not* invariant: the block swap sends an eigenvector  $(x, y)$  of  $\mathcal{H}(\mathcal{M})$  to  $(y, x)$ , so an eigenvector statistic that reads the query and key blocks separately (using token roles or temporal coordinates) can break the invariance. The corollary therefore covers eigenvalue- and singular-value-based diagnostics, and only those eigenvector summaries that are themselves block-swap symmetric.  $\square$

**Proposition 8 (Converse: asymmetry bounds transpose discrepancy)** For any  $L$ -Lipschitz functional  $F$  on  $(\mathbb{R}^{n \times n}, \|\cdot\|_F)$ ,

$$|F(\mathcal{M}) - F(\mathcal{M}^\top)| \leq 2L \|\mathcal{M}_{\text{asym}}\|_F. \quad (5)$$

In particular, if  $F(\mathcal{M}) \neq F(\mathcal{M}^\top)$ , then  $\|\mathcal{M}_{\text{asym}}\|_F \geq |F(\mathcal{M}) - F(\mathcal{M}^\top)| / (2L)$ .

**Proof.** Since  $\mathcal{M}^\top = \mathcal{M}_{\text{sym}} - \mathcal{M}_{\text{asym}}$ , we have  $\mathcal{M} - \mathcal{M}^\top = 2\mathcal{M}_{\text{asym}}$ , so  $\|\mathcal{M} - \mathcal{M}^\top\|_F = 2\|\mathcal{M}_{\text{asym}}\|_F$ . The Lipschitz bound gives  $|F(\mathcal{M}) - F(\mathcal{M}^\top)| \leq L\|\mathcal{M} - \mathcal{M}^\top\|_F = 2L\|\mathcal{M}_{\text{asym}}\|_F$ .  $\square$

Together with Theorem 5, this establishes a quantitative duality: symmetric spectral diagnostics are transpose-invariant (orientation blind), while any diagnostic that *does* distinguish  $\mathcal{M}$  from  $\mathcal{M}^\top$  must pay a cost proportional to  $\|\mathcal{M}_{\text{asym}}\|_F = G(\mathcal{M}) \cdot (\|\mathcal{M}\|_F + \varepsilon)$ . When  $G$  is small across a model’s attention heads, the converse guarantees that *no* Lipschitz diagnostic, symmetric or not, can achieve large transpose-sensitivity. The dominance of the capacity axis reflects the operator structure itself, not a design artifact. Proposition 8 holds for any  $L$ -Lipschitz functional on  $(\mathbb{R}^{n \times n}, \|\cdot\|_F)$ ; we use it here solely as a structural converse, not as a characterization of all useful diagnostics. The coefficient  $G$  therefore serves as the control parameter for transpose sensitivity: small  $G$  means all diagnostics are approximately orientation-blind, regardless of whether they use the Hermitian dilation.

**The minimal directional complement.** The orthogonal decomposition motivates a natural complement to conductance.  $G$  is the minimal complement required to recover directional information discarded by symmetric summaries, not primarily an empirical tool but a structural certificate that the symmetric and antisymmetric axes together span the transport operator’s Frobenius-orthogonal decomposition:

$$G(\mathcal{M}) = \frac{\|\mathcal{M}_{\text{asym}}\|_F}{\|\mathcal{M}\|_F + \varepsilon} = \frac{d(\mathcal{M}, \mathcal{S})}{\|\mathcal{M}\|_F + \varepsilon}, \quad (6)$$

where  $d(\mathcal{M}, \mathcal{S})$  is the Frobenius distance to the symmetric subspace. Its extremes pin down the structural meaning of the antisymmetric axis.

**Proposition 9 (Range and extremes of  $G$ )** *For any  $\mathcal{M}$ ,  $G(\mathcal{M}, 0) \in [0, 1]$ , with  $G = 0$  iff  $\mathcal{M}$  is symmetric and  $G = 1$  iff  $\mathcal{M}$  is purely skew ( $\mathcal{M}^\top = -\mathcal{M}$ ). A non-negative attention matrix cannot be purely skew, so  $G < 1$ ; within the causal class the antisymmetric-maximal pattern is strict lower-triangular (zero diagonal), where  $G = 1/\sqrt{2}$  exactly, and every causal Toeplitz operator obeys  $G \leq 1/\sqrt{2}$ .*

The symmetry claim is immediate from (6) ( $G = 0 \iff \mathcal{M}_{\text{asym}} = 0 \iff \mathcal{M} = \mathcal{M}^\top$ ); the causal  $1/\sqrt{2}$  ceiling follows from the Toeplitz structure of  $\mathcal{M}_{\text{asym}}$ . Full proofs are in Appendix C.

**Remark 10 (Optimality of  $G$ )** *Among diagnostics of the form  $D(\mathcal{M}) = \|\mathcal{M} - S\|_F / \|\mathcal{M}\|_F$  with  $S \in \mathcal{S}$ , the minimum is attained uniquely at  $S = \mathcal{M}_{\text{sym}}$  and equals  $G(\mathcal{M}, 0)$ .  $G$  therefore measures the minimal normalized Frobenius perturbation required to reach the transpose-invariant class.*

A geometric illustration of how  $G$  captures orientation failures that  $\hat{\phi}$  misses appears in the Online Supplement.

This closes the structural analysis of the symmetric–antisymmetric boundary:  $\phi$  and  $\sigma_2$  measure symmetric capacity,  $G$  measures the antisymmetric residual, and the converse bounds what any Lipschitz diagnostic can achieve beyond this decomposition. The next section develops  $G$ 's properties under causality and positional encoding, and synthesizes the three-axis diagnostic system.

## 5 Transport Diagnostics

The orientation-blindness theorem in Sec. 4 identifies  $G = \|\mathcal{M}_{\text{asym}}\|_F / (\|\mathcal{M}\|_F + \varepsilon)$  as the residual that any directional diagnostic must access. Two questions follow. First, when is  $G > 0$  guaranteed? Causal masking turns out to force  $G > 0$  for any non-trivial attention pattern, so the question becomes quantitative: how large is  $G$  as a function of the architecture's positional structure? Second, given conductance,  $\sigma_2$ , and  $G$ , what diagnostic system do they jointly form? This section answers both, then closes by also defining the empirical conductance estimator  $\hat{\phi}$  used in the experiments.

**Symmetry and causal structure.** The vanishing locus  $G = 0$  is exactly the symmetric subspace  $\mathcal{M} = \mathcal{M}^\top$ . In a graph-theoretic reading of the bipartite operator, this corresponds to the case where the random walk on  $\mathcal{H}(\mathcal{M})$  is reversible after volume normalisation Chung [2005]. Causal attention falls outside this locus by construction: lower-triangular support cannot be symmetric (except trivially), so a healthy causal attention head must have  $G > 0$ .

**Geometric constraint under causality.** For causal self-attention, the interpretation of  $G = 0$  is determined by a geometric constraint. Any lower-triangular  $\mathcal{M}$  with off-diagonal mass has  $(\mathcal{M}_{\text{asym}})_{ij} = \mathcal{M}_{ij}/2 \neq 0$  for  $i > j$  (since  $\mathcal{M}_{ji} = 0$  by the causal mask). Therefore, healthy causal attention necessarily has  $G > 0$ .

**Proposition 11 (Causal attention implies  $G > 0$ )** *For causal self-attention, the intersection of symmetric and lower-triangular is diagonal. Therefore  $G = 0$  implies temporal isolation, where each token attends only to itself.*

An illustration of the two failure modes (bottleneck and diffuse) and how they coexist in causally masked self-attention is provided in the Online Supplement.

**Quantitative bounds from positional structure.** Decoder models exhibit  $G$  well above the qualitative  $G > 0$  floor: Pythia, for instance, reaches  $G \approx 0.5$ – $0.65$ . Two *distinct* structural mechanisms can raise  $G$ , and they yield bounds of different strength. The first is a *monotone primacy profile*: rows whose weight decreases from the earliest key toward the diagonal. The second is a *first-token mass floor*: every query retaining a fixed fraction of attention on the earliest key at all sequence lengths, the attention-sink pattern documented across decoder language models [Xiao et al., 2024]. Softmax preserves monotone order in the pre-softmax logits, and the causal Toeplitz–Frobenius identity converts either profile into an antisymmetric-energy statement. The two mechanisms give the bounds below; *they are independent: the second is not a consequence of the first*. The supporting softmax-order and Toeplitz–Frobenius lemmas, and the proofs of these bounds, are in the Online Supplement, §17:

**Proposition 12 (Monotone primacy decay gives an  $O(1/\sqrt{n})$   $G$  bound)** *For a causal, row-stochastic matrix with monotone decreasing rows (weight largest at the earliest key) and  $n \geq 2$ :  $G(\mathcal{M}, \varepsilon) \geq 1/(4\sqrt{n} + 4\varepsilon)$ .*

**Proposition 13 (First-column mass floor gives an  $n$ -independent  $G$  bound)** *If a causal, row-stochastic matrix satisfies a first-column mass floor  $\mathcal{M}_{i,0} \geq c > 0$  for every row  $i \geq 1$ , then  $G(\mathcal{M}, 0) \geq c/2$ , independent of sequence length.*

**Corollary 14 (Exponential decay:  $n$ -independent  $G$  bound)** *For exponential decay  $f(k) = Ce^{-\alpha k}$  with  $\alpha > 0$ , every row satisfies the first-column floor  $\mathcal{M}_{i,0} \geq 1 - e^{-\alpha}$ . By Theorem 13,  $G(\mathcal{M}, 0) \geq (1 - e^{-\alpha})/2$ , independent of sequence length.*

The two bounds describe genuinely different regimes. A monotone primacy profile alone guarantees only  $G > 0$  with an  $O(1/\sqrt{n})$  rate, because the lower bound on antisymmetric energy rests on a single matrix entry. A first-column mass floor (the attention-sink structure) instead makes the antisymmetric energy grow as  $\Theta(n)$ , cancelling the  $\Theta(n)$  growth of  $\|\mathcal{M}\|_F^2$  and leaving a constant. It is the sink mechanism, not recency bias, that underwrites a sequence-length-independent floor on  $G$ ; recency decay (as induced by RoPE Su et al. [2024]) raises attention toward the diagonal and is a separate effect. This dependence on architectural structure (conductance is universal while a tight  $G$  bound requires a first-token floor) is the cost of the tighter bound; we return to this tradeoff in Sec. 8.

**Architecture-dependent interpretation.** The geometric constraint explains why  $G$  has different diagnostic value across architectures:

- **Decoder self-attention** (causal):  $G = 0$  implies symmetric, and symmetric  $\cap$  causal = diagonal. Therefore  $G = 0$  indicates temporal isolation, a *failure mode*.
- **Encoder self-attention** (bidirectional):  $G = 0$  requires only  $\mathcal{M} = \mathcal{M}^\top$ , achievable with arbitrary off-diagonal structure. This is *normal operation*, not pathological.

For encoder-decoder models,  $G$  should be interpreted as a temporal isolation diagnostic *only for decoder self-attention*.

**Empirical conductance estimator.** Exact conductance minimization is NP-hard [Šíma and Schaeffer, 2006], so we use a spectral sweep on the second singular vectors of  $\mathcal{M}$  (equivalently, the second eigenvector of  $\mathcal{H}(\mathcal{M})$ ) to obtain an empirical estimate  $\hat{\phi}$ . The sweep evaluates  $O(n_q + n_k)$  candidate threshold cuts; its approximation ratio is unbounded in the worst case but empirically within  $2\times$  on matched nulls. In practice, most heads lie within their intrinsic spectral band; rather than relying on literal “violations”, we use  $\hat{\phi}$  as a continuous structural score whose interpretation is anchored by the classical Cheeger inequality [Cheeger, 1970, Chung, 1997]. For causally masked matrices, the sweep operates

on the lower-triangular support; the bipartite Hermitian dilation  $\mathcal{H}(\mathcal{M})$  is always square ( $n_q + n_k$ ), so the procedure applies unchanged to rectangular cross-attention (Theorem 2).

**Diagnostic synthesis.** Together,  $\hat{\phi}$ ,  $\sigma_2$ , and  $G$  form a structurally grounded diagnostic system:  $\hat{\phi}$  provides a theory-grounded capacity certificate via the Cheeger inequality;  $\sigma_2$  captures coupling structure beyond degree heterogeneity (Theorem 3);  $G$  captures the antisymmetric residual that no symmetric method can access (Theorem 5). Alternative matrix norms ( $G_{\text{op}}$ ,  $G_*$ , KL-divergence rate of the induced random walk) partially strengthen the asymmetry signal in encoder-decoder architectures but do not achieve cross-architecture consistency (Online Supplement, §12). The diagnostic scope of  $G$  (where it discriminates and where it does not) is assessed empirically in Sec. 7.

The three diagnostics are defined. Before reporting results, we establish the evaluation protocol required to interpret them without length confounding.

## 6 Evaluation Protocol

Before the transport framework can be tested empirically, a methodological threat must be addressed: spectral features inherit length dependence that can inflate apparent discrimination. We characterize three distinct confounding channels and establish a length-controlled evaluation protocol that governs all subsequent empirical claims.

When hallucination rate correlates with response length (HaluEval:  $r=+0.70$ ,  $p<10^{-30}$ ; MedHallu:  $r=-0.21$ ,  $p=0.037$ ; TruthfulQA:  $r=-0.13$ ,  $p=0.057$ ), any feature that implicitly encodes length will appear discriminative even if it carries no semantic signal. We organize length confounding into three channels, using LLM-Check’s [Sriramanan et al., 2024] feature families (hidden-state, attention, output) as the organizing scaffold.

### 6.1 Three Channels of Length Exposure

**Hidden-state channel.** Methods that analyze covariance spectra of hidden representations inherit length dependence through centering and normalization: LLM-Check’s centering matrix produces  $\log(n-1)$  scaling in its mean log-eigenvalue score, and EigenTrack’s [Ettori et al., 2025] Marchenko–Pastur reference law depends on the aspect ratio  $\gamma = D/n$ , whose edges shift with  $n$ .

**Attention channel.** Methods that read statistics off attention matrices suffer position–length coupling: LLM-Check’s diagonal feature has  $\mathbb{E}[A_{ii}] = 1/i$  under causal masking ( $O(\log n/n)$  dependence) and discards off-diagonal routing structure, and LapEigvals [Binkowski et al., 2025] couples position to length through its degree matrix. In cross-attention ( $n_q \neq n_k$ ), growing query count with keys fixed scales column degrees, adding explicit length dependence (Proposition 15, Appendix B).

**Output channel.** Token-level entropy and perplexity are relatively robust (means converge with  $O(1/n)$  variance) though entropy extrema carry  $O(\log n)$  order-statistic effects. This channel has the mildest exposure but still warrants control. Per-method length-dependence derivations for LLM-Check, EigenTrack, and LapEigvals are in the Online Supplement, §6 and §8.

### 6.2 Length-Controlled AUROC

The three-channel taxonomy explains why different spectral methods behave inconsistently across benchmarks: without explicit length control, structural exposure remains and cross-

benchmark generalization suffers. Table 4 summarizes the evaluation metrics used throughout; formal definitions appear in the Online Supplement, §16.

**Length-controlled AUROC (LC-AUROC).** To control for length confounding at two levels, we partition samples by *response length* (model-specific tokenizer, excluding prompt) into  $B$  equal-frequency bins, where  $B$  is chosen adaptively per data set as the smallest value satisfying: (i) all bins contain  $\geq 25$  positive-negative pairs, (ii) no bin is degenerate, and (iii) the maximum within-bin Spearman rank correlation between score and length satisfies  $|\rho_b| < 0.10$ . Within each bin  $b$ , scores are residualized via OLS against length ( $r_i = s_i - \hat{s}_i$ ) to remove residual within-bin linear correlation, and per-bin AUROC values are aggregated with pair-weighting:<sup>2</sup>

$$\text{AUROC}_{\text{LC}} = \sum_b w_b \cdot \text{AUROC}_b(y, r_b), \quad (7)$$

$$w_b = \frac{n_{+,b} \times n_{-,b}}{\sum_{b'} n_{+,b'} \times n_{-,b'}}.$$

Pair-weighting ensures bins with class imbalance have appropriately reduced influence. Because a transport feature can discriminate with either polarity (high or low values flagging hallucination), we report *flipped* LC-AUROC,  $\max(\text{AUROC}(s), 1 - \text{AUROC}(s))$ . Flipping selects the polarity using the labels, so a flipped value answers “does this feature carry signal” rather than “does a label-free detector exist”: the features themselves are computed without labels, but a deployable detector additionally needs a small calibration set to fix the sign and threshold (Sec. 8). Unless stated otherwise, reported LC-AUROC values are flipped, and should be read as evidence of signal strength rather than as the accuracy of a deployed label-free classifier. Feature rankings under LC-AUROC are robust to hyperparameter choices: across a grid of bin counts and correlation thresholds, the mean Kendall  $\tau$  between feature rankings exceeds 0.75 for the majority of configurations (see Online Supplement, §9).

A representative per-quartile breakdown for GPT-2 on HaluEval, including bootstrap CIs and the raw vs. residualized vs. LC-AUROC comparison that motivates LC-AUROC, is shown in the Online Supplement (§4).

**Datasets and models.** We evaluate on three benchmarks chosen to span distinct length-label correlation regimes: HaluEval [Li et al., 2023] ( $n=10,000$ ;  $r_\ell=+0.70$ , strong positive), TruthfulQA [Lin et al., 2022] ( $n=817$ ;  $r_\ell=-0.13$ , near-zero), and MedHallu [Pandit et al., 2025] ( $n=1,000$ , the expert-labelled subset of the MedHallu benchmark;  $r_\ell=-0.21$ , weak negative). Spectral diagnostics are extracted by *forced scoring*: each prompt is concatenated with the benchmark-provided reference response (factual or hallucinated) and passed through the model in a single forward pass with attention outputs enabled; the models under study generate no text, so our claims concern internal processing of labelled responses rather than online generation dynamics, and are associational rather than causal (Sec. 8). Zero-shot methods (OC: conductance  $\hat{\phi}$ ; AG: asymmetry coefficient  $G$ ; LLM-Check) are evaluated on a 30% held-out test split; our EigenTrack port uses 5-fold cross-validation with a linear classifier (logistic regression with dropout 0.1). Models include GPT-2 and Pythia (decoder-only), BERT (encoder-only), and Flan-T5 (encoder-decoder with cross-attention and decoder self-attention); LLaMA-3.1-8B (decoder-only, grouped-query attention) is evaluated separately as a modern-model generalization check (Sec. 7.5). We evaluate using bootstrap confidence intervals (1000 samples, 95% CI) on 15 model-dataset combinations. All empirical claims in this paper use LC-AUROC as the primary metric, with raw AUROC reported only for

<sup>2</sup>Despite the two-stage structure (stratification then residualization), LC-AUROC is not a semiparametric doubly-robust estimator in the sense of Robins et al. [1994]: it does not guarantee consistency under misspecification of either the propensity or outcome model.

comparability. Features are aggregated across all layers and heads using CVaR (conditional value-at-risk; Rockafellar and Uryasev, 2000) and robust statistics (mean, median, std, IQR, range), eliminating hyperparameter tuning while improving generalization. As above, reported values use label-informed polarity; deployment additionally requires polarity and threshold calibration (Sec. 8).

**Baseline method limitations.** Some method–architecture combinations are undefined and marked “—” in Table 5: (i) *Cross-attention baselines*: LLM-Check and EigenTrack analyze self-attention or hidden states; cross-attention is not supported by these methods. (ii) *Encoder-only logit entropy*: BERT lacks autoregressive token prediction, so LLM-Check logit features are undefined. (iii) *Asymmetric guessing ( $G$ ) for cross-attention*: The Hermitian decomposition requires square attention matrices; cross-attention matrices are rectangular ( $n_q \neq n_k$ ), making  $G$  undefined.

### 6.3 Empirical Illustration

We validate this analysis on a composite design set (900 samples: 300 HaluEval, 300 TruthfulQA, 300 MedHallu). Response length alone achieves AUROC 0.96 on HaluEval, 0.74 on MedHallu, and 0.56 on TruthfulQA, confirming length is a strong univariate predictor where correlation exists. Spectral features inherit this confounding:  $\lambda_2$  shows  $r = 0.78$  correlation with length on GPT-2, and normalizing by  $\sqrt{n}$  over-corrects to  $r = -0.61$ , indicating finite-size effects; the Online Supplement (§10) gives the per-method length-confounding derivations and why random-matrix theory fails for attention.

With LC-AUROC defined and confounding channels characterized, we report results organized around the three research questions.

## 7 Empirical Results

With the transport framework defined (Secs. 2–5) and the evaluation protocol established (Sec. 6), we test three research questions. The experiments characterize what each diagnostic axis measures in practice: where it carries signal, what structural features drive that signal, and what it structurally cannot detect. AUROC serves as quantitative evidence for these structural characterizations, not as an end in itself; where we name a candidate mechanism, we mark it as a hypothesis consistent with the patterns rather than a demonstrated cause.

### 7.1 Q1: Does the Symmetric Axis Capture Capacity Failures under Length Control?

**Response-length baseline.** Response length alone achieves raw AUROC of 0.96 on HaluEval, 0.74 on MedHallu, and 0.56 on TruthfulQA (Sec. 6). Under LC-AUROC, response length collapses to  $\approx 0.50$  by construction, since within-bin residualization removes the signal that length provides. Transport features retain meaningful LC-AUROC (0.62–0.84), indicating that their discriminative power is not reducible to length encoding.

**Two failure regimes persist after length control.** Table 5 presents LC-AUROC for attention transport features aggregated across all layers and heads. CVaR tail analysis decomposes the conductance distribution into its structural extremes: high-conductance regions (CVaR<sub>75</sub>, top 25%) capture diffuse routing where attention dilutes across too many tokens; low-conductance regions (CVaR<sub>25</sub>, bottom 25%) capture over-constrained bottlenecks where attention concentrates on too few tokens. The diffuse tail produces a stronger hallucination signal (0.822 [0.798, 0.845]) than the bottleneck tail (0.617 [0.590,

0.645]), and overall spectral norm variability reaches 0.838 [0.815, 0.862] on HaluEval. This asymmetry (diffuse routing producing a stronger signal than bottleneck routing) is the central empirical pattern in these configurations.

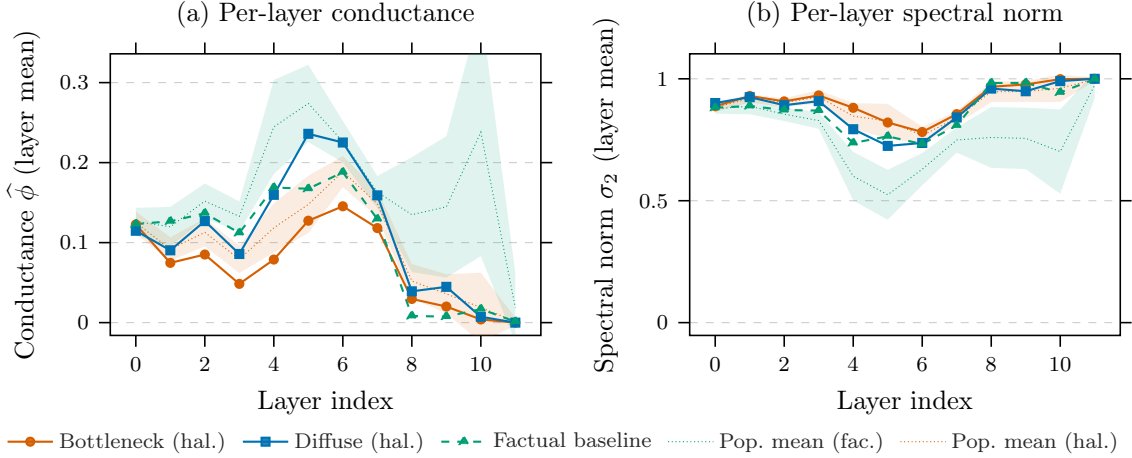


Figure 4: **Per-layer transport profiles reveal distinct failure signatures.** Conductance  $\hat{\phi}$  (a) and spectral norm  $\sigma_2$  (b) averaged across heads within each layer (Pythia-160M). Shaded bands show population  $\pm 1$  std around dotted mean lines (green: factual, red: hallucinated from HaluEval). **Bottleneck** (HaluEval, hallucinated): uniformly depressed  $\hat{\phi}$  and elevated  $\sigma_2$  across all layers—the spectral gap is small everywhere, indicating global over-concentration. **Diffuse** (MedHallu, hallucinated): elevated  $\hat{\phi}$  in middle layers with  $\sigma_2$  slightly lower—attention spreads too broadly. **Factual**: intermediate values within population bands.

Per-layer profiles are consistent with these failures being structurally distinct across the full transformer depth, rather than artifacts of individual layers (Figure 4): bottleneck samples show uniformly depressed  $\hat{\phi}$  across all 12 layers, while diffuse samples show selectively elevated  $\hat{\phi}$  in middle layers.

The conductance–spectral norm scatter (Figure 5) visualizes the polarity reversal between data sets: on HaluEval, hallucinations cluster at low  $\hat{\phi}$  (bottleneck); on MedHallu, at higher  $\hat{\phi}$  (diffuse).

Conductance also dissociates from simpler attention statistics: mean attention entropy and conductance are uncorrelated ( $\rho < 0.04$ ) and entropy itself has near-zero discriminative power (Cohen’s  $d = 0.04$  on HaluEval vs.  $d = -2.6$  for  $\hat{\phi}$ ), so conductance captures graph-theoretic transport structure not reducible to per-row entropy.

**Polarity variation reflects regime-dependent failure modes.** Between-dataset polarity variation is *consistent with* the two-sided theory and *supported* by tercile analysis. Stratifying samples by OC tercile reveals which failure mode dominates per data set. On HaluEval, hallucinations cluster in the *low*-OC tercile (mean 47.5% vs. 33% expected), consistent with bottleneck routing: attention over-concentrating on few tokens, missing relevant context. On MedHallu, hallucinations cluster in the *high*-OC tercile (mean 45.1%), consistent with diffuse routing: attention spreading too thinly, diluting relevance. The same diagnostic (OC) carries signal for failure in both cases; the *direction* of pathology differs. Full tercile distributions appear in the Online Supplement, §2. Matched null baselines (Sec. 3) confirm these signatures reflect learned structure rather than finite-size estimator artifacts: z-score normalization against entropy-matched and degree-preserving nulls improves AUROC by 6–8 points.

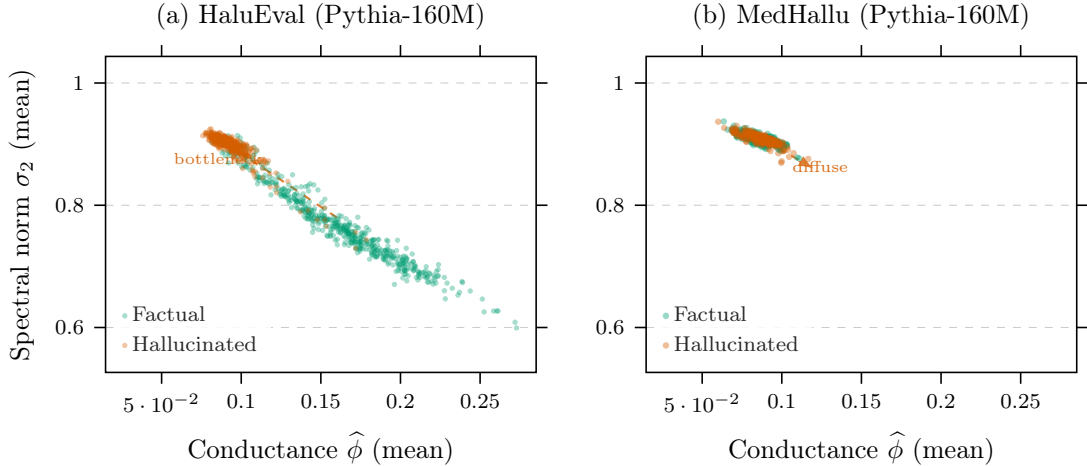


Figure 5: **Conductance–spectral norm scatter reveals regime-dependent polarity.** Each point is one sample; axes show conductance  $\hat{\phi}$  and spectral norm  $\sigma_2$  averaged across all heads and layers (Pythia-160M, 500 subsampled per class for HaluEval). The near-perfect anti-correlation ( $\rho=-0.99$ ) confirms the Cheeger inequality: low  $\hat{\phi}$  implies high  $\sigma_2$  (small spectral gap). **(a)** HaluEval: hallucinated samples cluster at low  $\hat{\phi}$  / high  $\sigma_2$  (bottleneck regime, Cohen’s  $d=-2.6$ ). **(b)** MedHallu: hallucinated samples shift toward higher  $\hat{\phi}$  / lower  $\sigma_2$  (diffuse regime, Cohen’s  $d=+0.3$ ). The polarity reversal between data sets visualizes the two-sided diagnostic: the same spectral signature detects opposite failure modes across data sets.

**Why the polarity reverses: the architectural-signature account.** The architectural-fraction analysis of Sec. 3 (Table 3) offers a structural account of the dataset-specific polarity reversal. Architectures differ distributionally in the fraction of heads piercing the 1/5 Cheeger floor (GPT-2 36–42%, Pythia-160M 55–70%, Flan-T5 decoder 79–82%), not head-by-head. HaluEval (hallucinations in the low-OC tercile) is the data set that exposes the bottleneck signal these heads carry, while MedHallu (hallucinations in the high-OC tercile) exposes the diffuse residual. Architectures with a larger bottleneck-regime fraction therefore polarise more on HaluEval; architectures with fewer leave more diffuse-signal weight and polarise more on MedHallu. The reversal is distributional, not per-head.

**Degree-preserving null decomposition.** Theorem 3 bounds the coupling-beyond-degree contribution to  $\sigma_2$  by  $\sqrt{\kappa} - 1$ , predicting that  $\sigma_2$  should retain signal once degree heterogeneity is controlled; the degree-preserving null decomposition tests this and supplies the complementary, empirical half about  $\hat{\phi}$ . Empirically (and this half is *not* predicted by the theorem), in the configurations studied  $\hat{\phi}$ ’s discriminative power is largely accounted for by the *degree distribution* (which tokens receive attention), with  $\hat{\phi}$  z-AUROC dropping to near chance (0.51–0.57) when degrees are preserved. As the theorem anticipates,  $\sigma_2$  retains substantial z-AUROC (0.72–0.80) under degree-preserving nulls, capturing coupling structure beyond degree heterogeneity (Theorem 3; degree-preserving nulls in the Online Supplement, §15.9). This decomposition is validated across length quartiles within each data set (ANOVA  $p > 0.05$ ), confirming that the degree-vs-coupling separation is not an artifact of sequence-length variation.

## 7.2 Q2: Does the Antisymmetric Axis Detect Directional Failures?

The asymmetric coefficient  $G$  shows weak discrimination for most configurations (0.53–0.63 LC-AUROC; Figure 6), indicating that temporal isolation is *not* the dominant failure mode

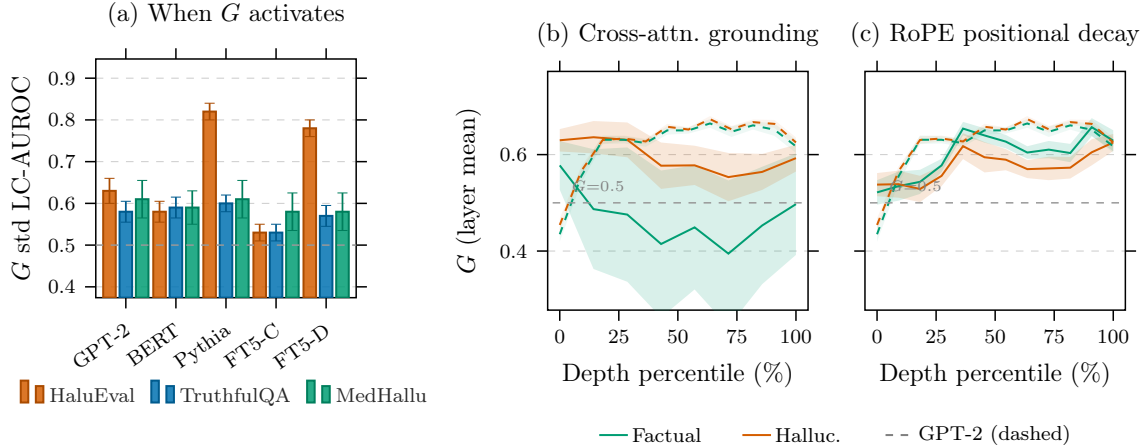


Figure 6: **Temporal isolation ( $G$ ) is sparse but architecture- and position-encoding-dependent.** (a) LC-AUROC for  $G$  std across all 15 model-dataset combinations with 95% bootstrap CIs. Most configurations cluster near chance; Flan-T5 decoder/HaluEval (0.78) and Pythia/HaluEval (0.82) are exceptions. (b) Per-layer  $G$  profiles on HaluEval (mean  $\pm 1$  std ribbons). Flan-T5 decoder (solid): clear class separation; factual  $G$  dips below 0.5 in middle layers, consistent with decoder self-attention relaxing toward symmetric transport when cross-attention grounding succeeds. GPT-2 (dashed): ribbons overlap (mean gap  $< 0.01$ ), the null case. (c) Pythia-160M (solid) shows *reversed polarity*: factual  $G >$  hallucinated  $G$  (mean gap  $-0.025$ ), concentrated in middle-to-late layers. This is consistent with a RoPE positional decay hypothesis: rotary embeddings impose a structured recency bias that factual generation must override to attend to earlier context, while hallucinated generation defaults to the decay pattern. GPT-2 (dashed, repeated as null reference) uses learned absolute positions and shows no such separation.

across the architectures studied. Two exceptions on HaluEval stand out: Flan-T5 decoder self-attention (0.78) and Pythia-160M (0.82).

The orientation blindness theorem (Theorem 5) is established by proof; the experiments characterize the conditions under which the antisymmetric axis carries discriminative signal. They do not test the theorem, which holds regardless of whether temporal isolation is currently active.

For Flan-T5, the pattern admits an interpretable hypothesis: decoder self-attention is informed by cross-attention to encoder representations, so its  $G$  profile may track whether grounding succeeds. Per-layer profiles (Figure 6b) show factual  $G$  dipping below 0.5 in middle layers, consistent with decoder self-attention relaxing toward symmetric transport when cross-attention provides adequate context. This separation is absent in GPT-2 (mean gap  $< 0.01$ ), which lacks an alternative information pathway, consistent with the architecture-dependent prediction of Proposition 11.

Pythia’s high  $G$  on HaluEval (0.82 [0.80, 0.84]) does not fit the encoder–decoder explanation: as a decoder-only model, it lacks cross-attention pathways. Per-layer profiles (Figure 6c) reveal a second finding: Pythia’s polarity is *reversed*; factual samples show *higher*  $G$  than hallucinated (mean gap  $-0.025$ ), concentrated in middle-to-late layers (4–10). A position-encoding hypothesis is consistent with this: Pythia’s rotary embeddings [Su et al., 2024] induce a recency bias that factual generation must override to retrieve earlier context, raising temporal directionality. GPT-2’s learned absolute embeddings carry no such systematic decay and show no separation (Figure 6c, dashed). The hypothesis is consistent but unconfirmed: the signal is dataset-specific (Pythia’s  $G$  is near chance on TruthfulQA 0.60 and MedHallu 0.61), and a response-length explanation does *not* account

for it: HaluEval responses are the *shortest* of the three benchmarks (median 7 tokens, versus 10 for TruthfulQA and 31 for MedHallu). The overall pattern is two distinct mechanisms: Flan-T5 decoder (high  $G$ , cross-attention grounding) and Pythia (high  $G$  with reversed polarity, candidate RoPE-recency mechanism).

**Feature-set ablation: the antisymmetric axis is empirically consequential, not only structurally necessary.** The orientation-blindness theorem guarantees that symmetric functionals cannot access  $\mathcal{M}_{\text{asym}}$ ; it does not by itself imply that the inaccessible component carries usable signal. Table 6 tests this directly, comparing logistic probes fit on the symmetric feature set  $\{\widehat{\phi} \text{CVaR}_{75}, \widehat{\phi} \text{CVaR}_{25}, \sigma_2 \text{ std}\}$  against the same set augmented with  $G$  std (5-fold out-of-fold scoring, the same supervised convention as the EigenTrack baseline; LC-AUROC throughout). Adding  $G$  yields CI-significant gains in 5 of 15 main-grid cells spanning three architectures, largest on Pythia/MedHallu ( $\Delta = +0.089 [+0.013, +0.126]$ ); notably, in the Llama-3.1-8B/HaluEval generalization cell  $G$  alone is near chance (0.539) yet still contributes  $\Delta = +0.025 [+0.014, +0.034]$  to the pooled probe—orientation information the symmetric axis does not carry. Cross-attention cells are neutral, as expected:  $G$  is unreliable for rectangular attention matrices (§3.6). One reversal occurs (Flan-T5 decoder on HaluEval,  $\Delta = -0.012 [-0.017, -0.008]$ ): there  $G$  alone is already strong (0.779), and the two axes carry overlapping rather than complementary signal in that configuration. The mean paired difference across the main grid is +0.012. The pattern matches the two-axis reading of the theory: the antisymmetric axis adds discriminative signal precisely where directional failure modes are active, and is inert where the theory predicts no orientation signal exists.

### 7.3 Q3: What Does Each Method Class Measure?

**Different diagnostic objects have structurally different length exposure.** Length confounding inflates raw AUROC by up to 0.28 points (compare with Table 5). The confounding structure is informative: spectral methods show substantial exposure ( $\Delta = +0.13$  for OC on Pythia/HaluEval), hidden-state features show moderate exposure ( $\Delta \approx +0.09$ ), and output entropy shows near-zero exposure ( $\Delta \approx -0.01$ ), as predicted by the intensive/extensive distinction (Sec. 6). Raw and per-quartile AUROC breakdowns appear in the Online Supplement (§1, §4).

**Hidden-state probes.** Hidden-state features detect *that* generation is unreliable without distinguishing *how*: they do not recover the bottleneck–diffuse–knowledge-gap taxonomy that the transport framework provides. Across 7 of 11 applicable configurations, LLM-Check hidden-state features achieve best or tied-best LC-AUROC (0.62–0.72), making them the strongest general-purpose discrimination signal, though one that is structurally agnostic to failure mode. Hidden features show substantial length confounding ( $\Delta \approx +0.09$ ); output entropy is length-robust ( $\Delta \approx -0.01$ ) but more variable (0.52–0.80 LC-AUROC).

**Learned classifiers.** Supervised spectral classifiers access the same diagnostic object (attention spectra) but through a learned lens, making them vulnerable to dataset-specific overfitting. EigenTrack achieves marginal signal on HaluEval for small models (GPT-2: 0.63, BERT: 0.62) but near-chance on TruthfulQA and MedHallu across most architectures (see Online Supplement, §7), consistent with overfitting to dataset-specific spectral signatures, though short-sequence effects cannot be excluded. Transport diagnostics (OC,  $G$ ) are zero-shot and provide interpretable failure mode characterization independent of training data size or dataset-specific tuning.

**TruthfulQA as stress test.** TruthfulQA induces near-uniform routing statistics across all methods (0.50–0.57), with hallucinations distributing uniformly across OC terciles ( $\approx 33\%$  each). Short responses (median 10 tokens) limit spectral observables, so the null hypothesis “spectral methods fail on short sequences” cannot be cleanly distinguished from “spectral methods correctly return null for non-routing failures.” We interpret the near-chance result as consistent with specificity (knowledge gaps produce no detectable routing pathology) while acknowledging that formal validation requires a data set with no length-label correlation, sufficiently long responses, and known knowledge-gap failures.

## 7.4 Summary

The evaluation supports a clear hierarchy of diagnostic roles:

- *Conductance* ( $\hat{\phi}, \sigma_2$ ): captures capacity failures (bottleneck vs. diffuse routing) with strong LC-AUROC (0.62–0.84) and interpretable failure mode characterization via CVaR tails.
- *Temporal isolation* ( $G$ ): principled axis that is empirically sparse in most configurations (0.53–0.63) with two HaluEval exceptions consistent with two hypothesized mechanisms: Flan-T5 decoder (0.78, cross-attention grounding) and Pythia (0.82, reversed polarity consistent with RoPE positional decay).
- *Hidden-state probes*: strongest general-purpose discrimination (0.62–0.72 LC-AUROC) but structurally agnostic to failure mode; moderate length confounding.
- *Specificity*: near-chance on TruthfulQA is consistent with the framework not hallucinating signal for non-routing failures, though finite-size effects at median 10 tokens cannot be excluded.

The contribution is not a single best-performing method but a principled framework that characterizes *how* attention routing fails, complementing output-based measures with structural routing analysis.

## 7.5 Generalization to a Modern Model

To test whether the transport diagnostics generalize beyond the GPT-2 and Pythia decoders, we evaluate LLaMA-3.1-8B (decoder-only, grouped-query attention, RoPE; roughly an order of magnitude larger than the headline decoders), extracted with the same spectral-sweep conductance estimator and the same length-controlled protocol. We report transport diagnostics only: the LLM-Check and EigenTrack baselines were not run on this model. The capacity axis retains signal at 8B scale ( $\sigma_2$  std and  $\hat{\phi}$  CVaR<sub>75</sub> reach 0.66–0.72 LC-AUROC on HaluEval), while the asymmetry axis  $G$  stays near chance, mirroring the sparse- $G$  pattern of the main results (Table 7). Signal is strongest on HaluEval and weaker on the smaller TruthfulQA and MedHallu splits, consistent with the length-confounding regime structure characterized above.

## 8 Discussion and Implications

Attention routing failures fall into qualitatively different shapes (bottleneck and diffuse) and distinguishing them is a question about which mathematical object a diagnostic analyses, not about which statistic is extracted from it. The symmetric–antisymmetric partition is a consequence of Hilbert–Schmidt orthogonality, not a design choice; the orientation-blindness theorem identifies which axis each diagnostic inhabits (Theorems 5 and 8), the closed-form bipartite-Cheeger landscape supplies the architectural benchmark for the symmetric axis (Theorems 19 and 20), and the empirical results characterise where each axis carries signal in practice. The two-axis diagnostic  $(\phi, G)$  that follows produces a falsifiable polarity prediction (bottleneck routing on HaluEval, diffuse routing on MedHallu), borne out under length-controlled evaluation on the tested decoder-only models and encoder–decoders.

## 8.1 What the Framework Provides

A single spectral statistic such as  $\sigma_2$  is straightforward to extract from a single SVD; the framework’s contribution is to answer five questions about routing structure that a single statistic does not address:

1. The two-sided conductance theory accounts for polarity variation across datasets (bottleneck routing on HaluEval, diffuse routing on MedHallu), giving a structural mechanism for the prediction.
2. CVaR tail analysis separates bottleneck from diffuse routing failures, distinguishing failure modes that share a common spectral footprint.
3. The relative ordering of  $\sigma_2$  and  $\hat{\phi}$  in LC-AUROC is consistent with the Cheeger inequality  $\phi^2/2 \leq 1 - \sigma_2 \leq 2\phi$ , which predicts that  $\sigma_2$  bounds conductance variability, a structural explanation grounded in the framework.
4. The degree-sufficiency finding (that  $\hat{\phi}$  is largely a proxy for the degree distribution while  $\sigma_2$  captures coupling beyond degrees) requires the framework to be stated: the degree-preserving null analysis presupposes that  $\hat{\phi}$  and  $\sigma_2$  measure different structural properties, a presupposition that the Cheeger inequality and degree-sufficiency theorem jointly provide.
5. The closed-form conductance landscape  $\phi(S_t) = tu(t) / \min(t(2+u(t)), 2n-t(2+u(t)))$  for uniform causal attention (Theorems 17 and 19) turns the existence claim “some cut has conductance bounded below” into a per-cut architectural signature: the position and depth of every cut’s conductance is predicted in closed form for the object  $\phi$ , and deviations of the measured estimator  $\hat{\phi}$  are read as architectural properties of position-encoding (Table 3).

The degree sufficiency finding is regime-dependent: it is strongest where length-label correlation exists (HaluEval), holds at intermediate lengths (MedHallu), and is structurally unfalsifiable on very short responses where all methods return null.

**$\sigma_2$  vs.  $\hat{\phi}$ : complementary rather than competing.** The degree-preserving null analysis reveals that  $\hat{\phi}$  and  $\sigma_2$  are partially redundant ( $\hat{\phi}$  is well-approximated by degree statistics) and partially complementary ( $\sigma_2$  retains signal under degree control). This decomposition identifies *what each feature measures*, a contribution that requires the framework to state.

**Diagnostic design: architecture determines observable.** The theoretical analysis identifies a tradeoff between architectural universality and signal strength: conductance  $\phi$  is *architecture-universal* (the Cheeger inequality, Eq. (3), holds for any weighted graph regardless of positional encoding or masking), whereas the asymmetric coefficient  $G$  is *architecture-dependent*, requiring knowledge of causal structure and positional encoding to guarantee signal (Theorems 12 to 14). In practice, this means  $\phi$  provides a reliable diagnostic baseline across architectures, while  $G$  carries a guaranteed sequence-length-independent floor when the architecture produces a first-token mass floor, the attention-sink pattern of decoder language models (Theorem 14). Aggregation across layers generalizes better than tuned layer windows, consistent with the theoretical prediction that routing failures manifest diffusely rather than at specific depths. Among aggregation methods, CVaR tails best capture the distributional structure of routing across heads.

Hidden-state spectral features such as those used in LLM-Check [Sriramanan et al., 2024] target a different observable (post-attention residual representations rather than the attention operator itself) and we observe a moderate length confound on this axis ( $\Delta \approx +0.09$ ); the orientation-blindness theorem applies specifically to spectral statistics of the degree-normalised attention operator and does not bear directly on hidden-state-based detection.

**G sparsity as a design-space constraint.** The empirical sparsity of  $G$  (0.53–0.63 LC-AUROC in most configurations) is itself an informative finding: it establishes that *orientation blindness is not a limitation of the diagnostic but a characteristic of the decoder-only architectures studied*. In the decoder-only models studied, attention asymmetry is dominated by positional structure (causal mask, attention sinks) rather than content-dependent directional routing. Alternative matrix norms ( $G_{\text{op}}$ ,  $G_*$ , entropy production rate) partially rehabilitate the asymmetry axis in encoder-decoder architectures but do not achieve cross-architecture consistency (Online Supplement, §12). The orientation blindness theorem (Theorem 5) guarantees that no symmetric method can access this axis, so  $G$ ’s sparsity is not evidence that the axis is unimportant; in the architectures studied, it indicates that content-dependent directional routing contributes little discriminative signal beyond architecture-specific positional effects. Architectures with explicit directional attention mechanisms would be expected to produce richer  $G$  signal.

**Practical calibration.** OC polarity is consistent across response-length bins in only roughly half of the model–dataset pairings (7 of 12), indicating that the sign of the diagnostic cannot be fixed a priori and must be calibrated per configuration. This reflects finite-size effects in spectral estimation: the variance of graph-spectral estimators on finite token sequences correlates negatively with response length (Spearman  $r = -0.55$ ), so short responses produce noisier estimates. Polarity calibration requires a modest calibration set of 50–100 examples per configuration; examining CVaR tails reveals whether high or low conductance predicts hallucination.

**Toward a taxonomy of attention by conductance landscape.** The closed-form cut and volume identities used to characterise uniform causal attention (Theorems 17 and 18) are not specific to that one architecture: the row-sum / column-sum decomposition of the bipartite-dilation cut and volume is a template that applies to *any* non-negative attention pattern. Each architecture admits its own closed-form  $\text{cut}(S_t)$  and  $\text{vol}(S_t)$ , derived from the row and column sums of its mask: window attention yields  $\text{cut}(S_t) \leq w$  (Theorem 16); exponential decay yields a geometric column-sum form; RoPE-style decay yields its own monotone family. Each closed form produces a distinct conductance-landscape shape, and the empirical signature in Table 3 is one slice of what we expect to be a broader taxonomy: *attention architectures classified by the geometry of their conductance landscape*, with bottleneck-regime fraction and worst-cut location as the two principal coordinates. The present paper proves the template for the canonical (uniform causal) case; extending the closed forms to other masks and decay structures is a natural next step that the framework supports without further infrastructure.

## 8.2 Limitations

**Association, not causation.** Matched null baselines (Sec. 3) separate estimator artifacts from learned structure, but do not exclude third-variable confounds. The degree sufficiency finding shows that  $\hat{\phi}$ ’s discriminative power is largely reducible to degree statistics; whether degree heterogeneity *causes* hallucination or merely co-occurs with it remains open.

**Forced scoring, not generation.** Every diagnostic is computed by passing a benchmark-provided response (factual or hallucinated) through the model in a single forward pass; the models under study generate no text (Sec. 6.2). Consequently we make no claim about online generation dynamics, and none of our results should be read causally: we do not claim that a routing geometry *produces* a hallucination, only that it *co-occurs* with the labelled response class after length control. Whether the same transport signatures arise

during autoregressive decoding, and whether intervening on them alters generated content, are separate empirical questions this design cannot answer.

**Scope.** We do not claim length is causally irrelevant to hallucination; we separate length-correlated from length-independent signal to identify what transport diagnostics contribute beyond what response length alone provides. Our analysis requires access to attention tensors, limiting applicability to API-only models. Diffuse, ungrounded attention (structurally healthy but semantically incorrect routing) remains undetectable by transport diagnostics alone. We do not claim the bottleneck–diffuse–knowledge-gap partition is exhaustive; value-projection errors, semantic drift, and other failure modes may produce hallucinations without detectable routing pathology.

**Scope of “zero-shot.”** The term “zero-shot” applies to *feature computation*: conductance,  $\sigma_2$ , and  $G$  are computed from attention matrices without any labeled training data. However, calibrated *decision-making* (determining whether a given conductance value indicates hallucination for a specific model-dataset configuration) requires a modest calibration set (50–100 labeled examples) to establish polarity and thresholds.

**Architecture coverage.** The data sets and models evaluated do not exhaust the space of modern architectures. The diagnostics generalize to LLaMA-3.1-8B (grouped-query attention, RoPE; Sec. 7.5), but sliding-window attention and mixture-of-experts routing remain untested.

**Value geometry and normalization.** Our transport-based diagnostics operate on attention matrices alone, remaining blind to value geometry and layer normalization in transformer blocks. Principled integration of these components (which govern how attention weights translate to representation updates) may improve diagnostic precision.

**Completeness.** The diagnostic decomposition characterizes the axes; whether both axes are active is an empirical question about the architecture, not a property of the framework.

**Future directions.** A directional spectral theory of attention that retains access to  $\mathcal{M}_{\text{asym}}$  at the spectral level remains open. Adjacent literatures supply partial analogs: magnetic-Laplacian Cheeger inequalities preserve direction via  $U(1)$  phases with a frustration-index RHS [Lange et al., 2015], and higher-order Hodge–Cheeger inequalities on simplicial complexes relate  $\lambda_k(\Delta_k)$  to coboundary expansion, one-sided for  $k \geq 1$  [Parzanchevski et al., 2016, Gundert and Szedlák, 2015]; the directed-Cheeger formalism of Chung [2005] restores reversibility by reweighting away the antisymmetric structure. Integrating any of these with the bipartite dilation  $\mathcal{H}(\mathcal{M})$  so that the resulting inequality preserves  $\mathcal{M}_{\text{asym}}$ , has a combinatorial RHS vanishing exactly when  $\mathcal{M}_{\text{asym}}$  is exact, and composes with the  $\phi$ -side analysis we have established, is, to our knowledge, open. A per-sample failure taxonomy (factual errors, context failures, semantic inconsistencies) would also enable validation of which diagnostic signals correspond to which failure types.

**Extension to mixture-of-experts routing.** The transport view is not limited to attention. In mixture-of-experts (MoE) transformers, token-to-expert dispatch defines a second bipartite routing operator, suggesting that conductance-style diagnostics may extend to expert bottlenecks, oversmoothing of specialization, and load-balancing pathologies. Unlike self-attention, however, expert routing is typically rectangular and lacks the causal symmetry structure required for our current asymmetry analysis, so extending the framework to MoE dispatch is a distinct problem.

The orientation-blindness theorem and the closed-form Cheeger landscape together establish that attention diagnostics partition by which axis they access, and the partition has architectural consequences that empirical conductance signatures can read. Where healthy routing is well-characterised, deviations carry mechanism; where the antisymmetric axis is sparse, that sparsity is itself an architectural property. Both axes (and the closed-form templates that anchor them) are open to extension to other masks, decay structures, and routing operators; the present paper proves the template for the canonical case.

## 9 Related Work

We conclude by situating the transport framework within the broader landscape of hallucination detection methods. The closest prior work (Lookback Lens [Chuang et al., 2024] and LapEigvals [Binkowski et al., 2025]) also analyzes attention, but without degree normalization (introducing length dependence) or orthogonal decomposition (conflating capacity and orientation failures). LLM-Check [Sriramanan et al., 2024] achieves competitive detection through hidden states but does not structurally distinguish routing failure modes. The transport framework’s contribution is not “better detection” but *diagnostic decomposition*: partitioning routing failures into interpretable, orthogonal axes with formal guarantees (Cheeger inequality, orientation blindness theorem) that explain what each axis can and cannot detect.

Hallucination detection methods differ in what internal object they analyze, how they extract discriminative signal, and what structural assumptions they make. We organize the landscape by *diagnostic object* (the representation from which the hallucination signal is derived), progressing from output-level (cheapest access, least structural insight) to transport-level (deepest structural insight, most constrained assumptions). This ordering reveals a fundamental tradeoff: methods with richer structural access can distinguish *how* generation fails, while lighter-weight methods can only flag *that* generation is unreliable.

### 9.1 Output-Level Methods

Output-level methods require only generation samples or token probabilities, making them applicable to black-box APIs.

**Self-consistency.** SelfCheckGPT [Manakul et al., 2023] generates multiple responses to the same prompt and uses inter-sample variance (measured via BERTScore, QA, or n-gram overlap) as a hallucination proxy. This approach is principled for *confabulations* (arbitrary incorrect generations) but misses *consistent* errors where the model reliably produces the same wrong answer. It also inherits the cost of multiple forward passes.

**Semantic entropy.** Farquhar et al. [2024] measure uncertainty at the *meaning* level by clustering sampled responses into semantic equivalence classes and computing entropy over these clusters. This addresses a fundamental limitation of token-level entropy: paraphrases of the same correct answer inflate token entropy without indicating unreliability. Semantic entropy achieves strong detection across tasks and generalizes to unseen prompts. However, it requires multiple generation passes and semantic similarity computation, and cannot distinguish failure *modes*: high semantic entropy indicates uncertainty, not the structural cause (routing failure vs. knowledge gap vs. calibration error).

### 9.2 External Verification

**Factual decomposition.** FActScore [Min et al., 2023] decomposes long-form generations into atomic factual claims and verifies each against Wikipedia, achieving high precision on

biographical generation. SAFE [Wei et al., 2024] extends this to search-augmented verification using language models as judges. These methods achieve high precision on factual claims but require external knowledge bases, scale poorly to real-time detection, and cannot assess claims outside the knowledge base’s coverage. Importantly, they evaluate *factual accuracy* rather than *generation process integrity*: a factually correct response generated through pathological routing would pass verification, while our transport diagnostics would flag the routing anomaly.

### 9.3 Internal-State Methods

Methods that probe hidden representations occupy an intermediate position: they access richer structure than output-level methods but do not model the attention mechanism’s routing function.

**Knowledge localization and hidden-state probes.** Feed-forward layers store factual associations as key-value memories [Geva et al., 2021, Meng et al., 2022], suggesting that some hallucinations arise from retrieval failures in MLP parameters rather than routing failures in attention, a distinction our framework makes explicit.

LLM-Check [Sriramanan et al., 2024] and INSIDE (EigenScore) [Chen et al., 2024] extract covariance spectra from hidden-state activations, using eigenvalue statistics as hallucination features. Both approaches capture population-level representational change correlated with hallucination and achieve strong detection performance (LLM-Check is best or tied-best in 7/11 model–dataset configurations in our evaluation; INSIDE is structurally analogous to LLM-Check’s hidden branch (both read eigenvalues of a hidden-state covariance matrix) and falls in the same orientation-blind class by Theorem 5). However, the signal indicates *that* generation is unreliable without distinguishing *how*: bottleneck routing, diffuse routing, and knowledge gaps all produce similar representational change. Hidden-state features also show substantial length confounding ( $\Delta \approx +0.09$  between raw and length-controlled AUROC; Sec. 6). The confound itself is established prior art: Santilli et al. [2025] formally prove that a shared length bias in the uncertainty score and the correctness function non-randomly skews AUROC rankings, and Janiak et al. [2025] show that simple response-length heuristics can match complex detectors under standard automatic evaluation; our length-controlled protocol operationalizes the control these works call for.

**Supervised spectral classifiers.** EigenTrack [Ettori et al., 2025] streams covariance-spectrum statistics of hidden activations into a learned (recurrent) classifier; because these statistics are referenced to a Marchenko–Pastur baseline with aspect ratio  $\gamma = D/n$ , they inherit irreducible length dependence (derivation in the Online Supplement, §7). In our evaluation, a linear-classifier port achieves marginal signal on HaluEval for small models (GPT-2: 0.63, BERT: 0.62) but near-chance on TruthfulQA and MedHallu.

### 9.4 Attention-Based Methods

Attention matrices encode the routing decisions that determine information flow through the transformer. A growing body of work analyzes attention patterns directly.

**Attention as grounding signal.** Lookback Lens [Chuang et al., 2024] identifies contextual hallucinations from the ratio of attention to context versus newly generated tokens, closest in spirit to our work, since both read hallucination signal from attention. Two differences matter. *Structurally*, it reduces each attention map to a single scalar, whereas the transport view treats the full operator  $\mathcal{M}$  and its  $\mathcal{M}_{\text{sym}}/\mathcal{M}_{\text{asym}}$  decomposition; the lookback ratio is itself transpose-invariant and falls in the orientation-blind class of Theorem 5. *Methodologically*, it

trains a supervised classifier on the lookback features, placing it outside the zero-shot regime that frames our empirical comparison; we therefore retain it as a related-work comparison rather than a baseline. Its orientation-blind prediction is testable independently of the classifier and would manifest as failure on the  $G$ -dominant Pythia/HaluEval regime.

**Attention head analysis.** Voita et al. [2019] demonstrate that multi-head attention exhibits functional specialization: a small number of heads perform critical functions (positional, syntactic, rare-word), while the majority can be pruned without performance degradation. This head specialization is relevant to our aggregation strategy: rather than pre-selecting critical heads (which would require supervised identification), we aggregate conductance across all heads using CVaR and robust statistics, capturing the distributional structure of routing quality across the full set of heads.

**Spectral attention phenomena.** Attention entropy collapse during training [Zhai et al., 2023] (where attention distributions sharpen to near-deterministic patterns) and doubly-exponential rank loss in deep self-attention [Dong et al., 2021] are spectral phenomena that affect the transport properties we measure. Nait Saada et al. [2025] provide a spectral analysis of rank collapse and signal propagation in attention layers, relating the spectral gap to how representations collapse in width. Our Cheeger inequality connection formalizes a complementary aspect: the spectral gap of the degree-normalized operator bounds conductance, which in turn bounds how quickly routing can mix information across token positions.

**Self-attention as a transport operator.** Geshkovski et al. [2023] analyse self-attention as a continuous mean-field transport flow on the sphere and prove that token representations cluster asymptotically. Their framing motivates the transport view we adopt: where they study *trajectories* of tokens under iterated attention, we study the *instantaneous spectral structure* of a single normalised attention map and ask which routing failures are detectable from it. The two analyses are complementary; our orientation-blindness theorem identifies a structural ceiling that any symmetric-spectral diagnostic of an attention transport step must respect, regardless of whether it is read off a single layer or aggregated across the dynamical trajectory. The operator-level reading of attention also has direct antecedents: Sinkformers [Sander et al., 2022] interpret Sinkhorn-normalized attention as a doubly stochastic transport plan between queries and keys, and Erel et al. [2025] analyze the row-stochastic attention matrix as a discrete-time Markov chain, deriving structural properties of its steady-state distribution. We adopt the same object but ask a different question: which routing failures its spectral geometry can and cannot certify.

**Attention asymmetry via SVD.** Primal-Attention [Chen et al., 2023] treats self-attention as an asymmetric kernel and applies kernel SVD to it, the published antecedent for taking the asymmetry of attention seriously as a spectral object. The delta is direction of use: they build a new attention mechanism on the asymmetric representation, whereas we prove limits of symmetric functionals of the existing mechanism and quantify the discarded component through  $G$ .

**Spectral features from attention maps.** Binkowski et al. [2025] extract graph-Laplacian eigenvalues ( $L = D - A$ ) from raw attention matrices as hallucination features. This inherits length dependence through the degree matrix  $D$  (whose trace grows with sequence length) and discards off-diagonal routing mass by Laplacian construction; our degree-normalized operator  $\mathcal{M} = D_Q^{-1/2} A D_K^{-1/2}$  absorbs the trace scaling by construction. We do not include LapEigvals as an empirical baseline, for two reasons. First, it is a supervised method:

it trains a probe on attention-map Laplacian eigenvalues and is evaluated under its own protocol, so a faithful port requires reproducing the full training protocol (probe training, candidate-eigenvalue subset, length-binning scheme), not a drop-in feature swap. Second, and more importantly, the orientation-blindness corollary (Theorem 7) applies to it structurally regardless of empirical performance: its features are functions of symmetrized spectra, and the Online Supplement (§8) derives this collapse explicitly. The structural argument is the claim this paper makes about LapEigvals; an empirical port would test the method, not the theorem.

## 9.5 Graph-Theoretic and Transport Perspectives

Our framework draws on spectral graph theory, connecting attention analysis to a mature mathematical tradition.

**Spectral graph theory foundations.** The Cheeger inequality [Cheeger, 1970, Chung, 1997] relates the spectral gap of a graph’s Laplacian to its conductance (minimum normalized cut). Originally developed for Riemannian manifolds, its discrete analogue underpins rapidly-mixing Markov-chain analysis [Sinclair and Jerrum, 1989] and provides the theoretical backbone of our conductance diagnostic: the two-sided bound  $\phi^2/2 \leq 1 - \sigma_2 \leq 2\phi$  (Eq. (3)) guarantees that spectral structure reveals transport failures. Higher-order extensions [Lee et al., 2014, Kwok et al., 2013] relate higher eigenvalues to multi-way partitioning; we restrict to the second singular value as it provides the most robust single diagnostic.

**Spectral clustering and random walks.** The mixing time–spectral gap connection [von Luxburg, 2007, Lovász, 1996, Levin et al., 2006] underlies our interpretation of conductance as a transport capacity measure. Our framework extends this to the non-reversible setting of causal attention, where the antisymmetric component  $\mathcal{M}_{\text{asym}}$  captures the departure from reversibility.

**Directed graph spectra.** Chung [2005] extends the Cheeger inequality to directed graphs, defining a circulation-based notion of conductance for non-reversible Markov chains. This is the natural setting for causal attention, where information flows forward in time. Meila and Pentney [2007] develops weighted cuts for directed graphs, and Fill [1991] provides eigenvalue bounds on convergence for non-reversible chains. Cucuringu et al. [2020] show that Hermitian (complex-valued) matrix representations of directed graphs recover the orientation structure that symmetrization destroys; we inherit this insight directly. What we contribute beyond it is the attention-specific blindness partition, naming the affected detectors (LLM-Check, EigenTrack, LapEigvals), together with the closed-form conductance landscape for canonical causal architectures. Our asymmetric coefficient  $G$  (Sec. 5) measures the degree of non-reversibility; the orientation blindness theorem (Theorem 5) proves that this quantity is structurally invisible to symmetric spectral methods, which is what motivates  $G$  as a necessary complement to conductance.

## References

Jakub Binkowski, Denis Janiak, Albert Sawczyn, Bogdan Gabrys, and Tomasz Jan Kajanowicz. Hallucination detection in LLMs using spectral features of attention maps. In *Proceedings of the 2025 Conference on Empirical Methods in Natural Language Processing (EMNLP)*, pages 24354–24385, Suzhou, China, 2025. Association for Computational Linguistics. doi: 10.18653/v1/2025.emnlp-main.1239.

- Jeff Cheeger. A Lower Bound for the Smallest Eigenvalue of the Laplacian. In Robert C. Gunning, editor, *Problems in Analysis: A Symposium in Honor of Salomon Bochner*, pages 195–199. Princeton University Press, Princeton, NJ, 1970. Princeton Legacy Library reprint: 2015, ISBN 978-1-4008-6931-2.
- Chao Chen, Kai Liu, Ze Chen, Yi Gu, Yue Wu, Mingyuan Tao, Zhihang Fu, and Jieping Ye. INSIDE: LLMs’ internal states retain the power of hallucination detection. In *The Twelfth International Conference on Learning Representations (ICLR 2024)*, 2024.
- Yingyi Chen, Qinghua Tao, Francesco Tonin, and Johan A. K. Suykens. Primal-attention: Self-attention through asymmetric kernel SVD in primal representation. In *Advances in Neural Information Processing Systems*, volume 36, 2023.
- Yung-Sung Chuang, Linlu Qiu, Cheng-Yu Hsieh, Ranjay Krishna, Yoon Kim, and James R. Glass. Lookback lens: Detecting and mitigating contextual hallucinations in large language models using only attention maps. In *Proceedings of the 2024 Conference on Empirical Methods in Natural Language Processing*, pages 1419–1436, Miami, Florida, USA, 2024. Association for Computational Linguistics. doi: 10.18653/v1/2024.emnlp-main.84.
- Fan R. K. Chung. *Spectral Graph Theory*, volume 92 of *CBMS Regional Conference Series in Mathematics*. American Mathematical Society, 1997. ISBN 978-0-8218-0315-8.
- Fan R. K. Chung. Laplacians and the Cheeger Inequality for Directed Graphs. *Annals of Combinatorics*, 9(1):1–19, April 2005. ISSN 0219-3094. doi: 10.1007/s00026-005-0237-z.
- Mihai Cucuringu, Huan Li, He Sun, and Luca Zanetti. Hermitian matrices for clustering directed graphs: Insights and applications. In *Proceedings of the 23rd International Conference on Artificial Intelligence and Statistics (AISTATS)*, volume 108 of *Proceedings of Machine Learning Research*, pages 983–992. PMLR, 2020.
- Yihe Dong, Jean-Baptiste Cordonnier, and Andreas Loukas. Attention is not all you need: Pure attention loses rank doubly exponentially with depth. In *Proceedings of the 38th International Conference on Machine Learning*, volume 139 of *Proceedings of Machine Learning Research*, pages 2793–2803. PMLR, 2021.
- Yotam Erel, Olaf Dünkler, Rishabh Dabral, Vladislav Golyanik, Christian Theobalt, and Amit H. Bermano. Attention (as discrete-time Markov) chains. In *Advances in Neural Information Processing Systems*, volume 38, 2025.
- Davide Ettori, Nastaran Darabi, Sina Tayebati, Ranganath Krishnan, Mahesh Subedar, Omesh Tickoo, and Amit Ranjan Trivedi. EigenTrack: Spectral activation feature tracking for hallucination and out-of-distribution detection in LLMs and VLMs. arXiv preprint arXiv:2509.15735, 2025.
- Sebastian Farquhar, Jannik Kossen, Lorenz Kuhn, and Yarin Gal. Detecting hallucinations in large language models using semantic entropy. *Nature*, 630(8017):625–630, June 2024. ISSN 1476-4687. doi: 10.1038/s41586-024-07421-0.
- James Allen Fill. Eigenvalue bounds on convergence to stationarity for nonreversible Markov chains, with an application to the exclusion process. *The Annals of Applied Probability*, 1(1):62–87, 1991. doi: 10.1214/aoap/1177005981.
- Borjan Geshkovski, Cyril Letrouit, Yury Polyanskiy, and Philippe Rigollet. The emergence of clusters in self-attention dynamics. In *Advances in Neural Information Processing Systems*, volume 36, pages 57026–57037, 2023.

- Mor Geva, Roei Schuster, Jonathan Berant, and Omer Levy. Transformer feed-forward layers are key-value memories. In *Proceedings of the 2021 Conference on Empirical Methods in Natural Language Processing (EMNLP)*, pages 5484–5495, 2021. doi: 10.18653/v1/2021.emnlp-main.446.
- Gene H. Golub and Charles F. van Loan. *Matrix Computations*. Johns Hopkins University Press, 4th edition, 2013. ISBN 978-1-4214-0794-4.
- Ronald L. Graham, Donald E. Knuth, and Oren Patashnik. *Concrete Mathematics: A Foundation for Computer Science*. Addison-Wesley, 2nd edition, 1994. ISBN 978-0-201-55802-9.
- Anna Gundert and May Szedlák. Higher dimensional discrete Cheeger inequalities. *Journal of Computational Geometry*, 6(2):54–71, 2015. doi: 10.20382/jocg.v6i2a4.
- Roger A. Horn and Charles R. Johnson. *Matrix Analysis*. Cambridge University Press, 2nd edition, 2012. ISBN 978-0-521-83940-2. doi: 10.1017/CBO9781139020411.
- Denis Janiak, Jakub Binkowski, Albert Sawczyn, Bogdan Gabrys, Ravid Shwartz-Ziv, and Tomasz Jan Kajdanowicz. The illusion of progress: Re-evaluating hallucination detection in LLMs. In *Proceedings of the 2025 Conference on Empirical Methods in Natural Language Processing*, pages 34728–34745, Suzhou, China, 2025. Association for Computational Linguistics. doi: 10.18653/v1/2025.emnlp-main.1761.
- Tsz Chiu Kwok, Lap Chi Lau, Yin Tat Lee, Shayan Oveis Gharan, and Luca Trevisan. Improved Cheeger’s inequality: Analysis of spectral partitioning algorithms through higher order spectral gap. In *Proceedings of the Forty-Fifth Annual ACM Symposium on Theory of Computing (STOC)*, pages 11–20. ACM, 2013. doi: 10.1145/2488608.2488611.
- Carsten Lange, Shiping Liu, Norbert Peyerimhoff, and Olaf Post. Frustration index and Cheeger inequalities for discrete and continuous magnetic Laplacians. *Calculus of Variations and Partial Differential Equations*, 54(4):4165–4196, 2015. doi: 10.1007/s00526-015-0935-x.
- James R. Lee, Shayan Oveis Gharan, and Luca Trevisan. Multiway spectral partitioning and higher-order Cheeger inequalities. *Journal of the ACM*, 61(6):1–30, 2014. doi: 10.1145/2665063. Conference version in STOC 2012.
- David A. Levin, Yuval Peres, and Elizabeth L. Wilmer. *Markov chains and mixing times*. American Mathematical Society, 2006.
- Junyi Li, Xiaoxue Cheng, Wayne Xin Zhao, Jian-Yun Nie, and Ji-Rong Wen. HaluEval: A large-scale hallucination evaluation benchmark for large language models. In *Proceedings of the 2023 Conference on Empirical Methods in Natural Language Processing*, pages 6449–6464, Singapore, 2023. Association for Computational Linguistics. doi: 10.18653/v1/2023.emnlp-main.397.
- Stephanie Lin, Jacob Hilton, and Owain Evans. TruthfulQA: Measuring how models mimic human falsehoods. In *Proceedings of the 60th Annual Meeting of the Association for Computational Linguistics (Volume 1: Long Papers)*, pages 3214–3252, Dublin, Ireland, 2022. Association for Computational Linguistics. doi: 10.18653/v1/2022.acl-long.229.
- L. Lovász. Random walks on graphs: A survey. In D. Miklós, V. T. Sós, and T. Szőnyi, editors, *Combinatorics, Paul Erdős is Eighty*, volume 2, pages 353–398. János Bolyai Mathematical Society, Budapest, 1996.

- Potsawee Manakul, Adian Liusie, and Mark J. F. Gales. Selfcheckgpt: Zero-resource black-box hallucination detection for generative large language models. In *Proceedings of the 2023 Conference on Empirical Methods in Natural Language Processing (EMNLP)*, pages 9004–9017, 2023. doi: 10.18653/v1/2023.emnlp-main.557.
- Marina Meila and William Pentney. Clustering by weighted cuts in directed graphs. In *Proceedings of the 2007 SIAM International Conference on Data Mining*, pages 135–144, 2007. doi: 10.1137/1.9781611972771.13.
- Kevin Meng, David Bau, Alex Andonian, and Yonatan Belinkov. Locating and editing factual associations in GPT. In *Advances in Neural Information Processing Systems*, volume 35, 2022.
- Sewon Min, Kalpesh Krishna, Xinxu Lyu, Mike Lewis, Wen-tau Yih, Pang Wei Koh, Mohit Iyyer, Luke Zettlemoyer, and Hannaneh Hajishirzi. FActScore: Fine-grained atomic evaluation of factual precision in long form text generation. In *Proceedings of the 2023 Conference on Empirical Methods in Natural Language Processing (EMNLP)*, pages 12076–12100, 2023. doi: 10.18653/v1/2023.emnlp-main.741.
- Thiziri Nait Saada, Alireza Naderi, and Jared Tanner. Mind the gap: A spectral analysis of rank collapse and signal propagation in attention layers. In *Proceedings of the 42nd International Conference on Machine Learning*, Proceedings of Machine Learning Research. PMLR, 2025.
- Shrey Pandit, Jiawei Xu, Junyuan Hong, Zhangyang Wang, Tianlong Chen, Kaidi Xu, and Ying Ding. MedHallu: A comprehensive benchmark for detecting medical hallucinations in large language models. In *Proceedings of the 2025 Conference on Empirical Methods in Natural Language Processing*, pages 2858–2873, Suzhou, China, 2025. Association for Computational Linguistics. doi: 10.18653/v1/2025.emnlp-main.143.
- Ori Parzanchevski, Ron Rosenthal, and Ran J. Tessler. Isoperimetric inequalities in simplicial complexes. *Combinatorica*, 36(2):195–227, 2016. doi: 10.1007/s00493-014-3002-x.
- James M. Robins, Andrea Rotnitzky, and Lue Ping Zhao. Estimation of regression coefficients when some regressors are not always observed. *Journal of the American Statistical Association*, 89(427):846–866, 1994. doi: 10.1080/01621459.1994.10476818.
- R. Tyrrell Rockafellar and Stanislav Uryasev. Optimization of conditional value-at-risk. *Journal of Risk*, 2(3):21–41, 2000.
- Michael E. Sander, Pierre Ablin, Mathieu Blondel, and Gabriel Peyré. Sinkformers: Transformers with doubly stochastic attention. In *Proceedings of the 25th International Conference on Artificial Intelligence and Statistics (AISTATS)*, volume 151 of *Proceedings of Machine Learning Research*, pages 3515–3530. PMLR, 2022.
- Andrea Santilli, Adam Golinski, Michael Kirchhof, Federico Danieli, Arno Blaas, Miao Xiong, Luca Zappella, and Sinead Williamson. Revisiting uncertainty quantification evaluation in language models: Spurious interactions with response length bias results. In *Proceedings of the 63rd Annual Meeting of the Association for Computational Linguistics (Volume 2: Short Papers)*, pages 743–759, Vienna, Austria, 2025. Association for Computational Linguistics. doi: 10.18653/v1/2025.acl-short.60.
- Jiří Šíma and Satu Elisa Schaeffer. On the NP-completeness of some graph cluster measures. In *SOFSEM 2006: Theory and Practice of Computer Science*, volume 3831 of *Lecture Notes in Computer Science*, pages 530–537. Springer, 2006. doi: 10.1007/11611257\_51.

- Alistair Sinclair and Mark Jerrum. Approximate counting, uniform generation and rapidly mixing Markov chains. *Information and Computation*, 82(1):93–133, 1989. ISSN 0890-5401. doi: 10.1016/0890-5401(89)90067-9.
- Gaurang Sriramanan, Siddhant Bharti, Vinu Sankar Sadasivan, Shoumik Saha, Priyatham Kattakinda, and Soheil Feizi. LLM-Check: Investigating detection of hallucinations in large language models. In *Advances in Neural Information Processing Systems*, volume 37, 2024.
- Jianlin Su, Murtadha Ahmed, Yu Lu, Shengfeng Pan, Wen Bo, and Yunfeng Liu. RoFormer: Enhanced transformer with rotary position embedding. *Neurocomputing*, 568:127063, 2024. doi: 10.1016/j.neucom.2023.127063.
- Ashish Vaswani, Noam Shazeer, Niki Parmar, Jakob Uszkoreit, Llion Jones, Aidan N. Gomez, Lukasz Kaiser, and Illia Polosukhin. Attention is all you need. In *Advances in Neural Information Processing Systems*, volume 30, pages 5998–6008, 2017.
- Elena Voita, David Talbot, Fedor Moiseev, Rico Sennrich, and Ivan Titov. Analyzing multi-head self-attention: Specialized heads do the heavy lifting, the rest can be pruned. In *Proceedings of the 57th Annual Meeting of the Association for Computational Linguistics*, pages 5797–5808, 2019. doi: 10.18653/v1/P19-1580.
- Ulrike von Luxburg. A tutorial on spectral clustering. *Statistics and Computing*, 17(4): 395–416, December 2007. ISSN 0960-3174. doi: 10.1007/s11222-007-9033-z.
- Jerry Wei, Chengrun Yang, Xinying Song, Yifeng Lu, Nathan Hu, Jie Huang, Dustin Tran, Daiyi Peng, Ruibo Liu, Da Huang, Cosmo Du, and Quoc V. Le. Long-form factuality in large language models. In *Advances in Neural Information Processing Systems*, volume 37, 2024.
- Guangxuan Xiao, Yuandong Tian, Beidi Chen, Song Han, and Mike Lewis. Efficient streaming language models with attention sinks. In *International Conference on Learning Representations (ICLR)*, 2024.
- Shuangfei Zhai, Tatiana Likhomanenko, Etai Littwin, Dan Busbridge, Jason Ramapuram, Yizhe Zhang, Jiatao Gu, and Joshua M. Susskind. Stabilizing transformer training by preventing attention entropy collapse. In *Proceedings of the 40th International Conference on Machine Learning*, volume 202 of *Proceedings of Machine Learning Research*, pages 40770–40803. PMLR, 2023.

Table 1: **Claim audit.** Each headline claim, the formal result that supports it, the empirical evidence, and the scope within which the claim holds. “Support” distinguishes results proved in this paper from claims that are *empirical* (no theorem predicts them). Throughout,  $\phi$  is the exact (NP-hard) conductance of the raw attention graph and  $\hat{\phi}$  its spectral-sweep estimator; reported LC-AUROC values use label-informed polarity and therefore measure *signal strength*, not deployed-detector accuracy (Sec. 6.2).

Claim	Support	Empirical evidence	Scope / limitation
Symmetric spectral diagnostics are orientation-blind.	Theorem 5; converse Theorem 8.	Proof; Theorem 7 lists affected methods (LLM-Check, EigenTrack, LapEigvals).	Bounds only transpose-invariant functionals of $\mathcal{M}_{\text{sym}}$ ; does not constrain hidden-state methods.
Conductance is a two-sided capacity axis (bottleneck vs. diffuse).	Theorem 4; Cheeger inequality.	Diffuse tail 0.822 [0.798, 0.845] vs. bottleneck tail 0.617 (HaluEval); terciles 47.5%/45.1%.	Measured via the estimator $\hat{\phi}$ , not the exact object $\phi$ ; the sweep ratio is empirically within $2\times$ on matched nulls.
Uniform causal attention obeys a floor $\phi \geq 1/5$ ; window attention pierces it as $O(w/n)$ .	Theorem 19, Theorem 20, Theorem 16.	Table 3: floor-violation fraction separates architectures (36–42% / 55–70% / 79–82%).	The floor is an <i>idealized-architecture</i> benchmark, not an empirical attractor; the <i>violation fraction</i> is the observable, not a theory failure.
Polarity is regime-dependent and reverses across benchmarks.	Falsifiable consequence of the two-sided theory.	Reversal HaluEval (low-OC) $\leftrightarrow$ MedHallu (high-OC); Fig. 5.	Label-informed flip selects polarity; within-dataset polarity is bin-consistent in only roughly half of model-dataset pairings (7 of 12), a signal-strength claim, not a deployed detector.
$\hat{\phi}$ is largely degree-reducible; $\sigma_2$ carries coupling beyond degree.	Theorem 3 supports the $\sigma_2$ half only.	Degree-preserving nulls: $\hat{\phi}$ z-AUROC 0.51–0.57 (chance); $\sigma_2$ 0.72–0.80.	The $\hat{\phi}$ -side reducibility is <i>empirical</i> ; Theorem 3 bounds only $\sigma_2$ ’s coupling term.
The antisymmetric axis $G$ is sparse but architecture-dependent.	Theorem 11, Theorem 13, Theorem 14 (floors under sink/decay).	$G$ 0.53–0.63 in most configurations; exceptions Flan-T5 0.78, Pythia 0.82 (HaluEval).	The proposed mechanisms (cross-attention grounding, RoPE recency) are <i>hypotheses consistent with</i> the patterns, not confirmed causes.
Transport features carry length-independent signal.	Length-controlled evaluation protocol (Sec. 6.2).	0.62–0.84 LC-AUROC after control; response length alone collapses to $\approx 0.50$ .	Computed under <i>forced scoring</i> of benchmark-provided responses; no claim about online generation dynamics.

Table 2: **Matched-null validation (entropy-matched, HaluEval)**. Spectral discrimination persists after z-scoring each sample against  $m=50$  entropy-matched nulls: the lower-baseline models gain 6–8 points, the rest stay near their ceiling. Hallucination samples therefore deviate *systematically* from their own null expectation, which rules out the objection that the signal is a finite-size estimator artifact. Full results (all benchmarks,  $\sigma_2$  and  $\tau$ , and the degree-preserving nulls that decompose the signal) are in the Online Supplement.

Architecture	$\hat{\phi}$ AUROC		$\sigma_2$ AUROC	
	raw	z-score	raw	z-score
BERT	0.69	0.77	0.70	0.79
GPT-2	0.70	0.75	0.73	0.72
Pythia-160M	0.97	0.94	0.98	0.96
Flan-T5 cross	0.97	0.97	0.97	0.92
Flan-T5 dec.	0.95	0.97	0.97	0.97

Table 3: **Empirical conductance-landscape summary**. Per-(model, data set) statistics over all (sample, layer, head) tuples (target 50 samples; subject to the  $n \geq 32$  length filter): the location  $t^*/n$  of the empirical worst cut, the estimator minimum  $\min_t \hat{\phi}(S_t)$  (the spectral-sweep estimate, not the exact object  $\phi$ ), and the fraction of tuples whose estimator falls below the 1/5 Cheeger floor predicted for the idealized uniform-causal object  $\phi$  by Theorem 20. The floor is a theoretical benchmark, not an empirical attractor; the violation fraction is the architectural observable. The floor-violation fraction carries a 95% *clustered* bootstrap CI (resampling unit: sample; 5000 resamples), since (layer, head) tuples within a sample are correlated and a binomial interval over all  $n_{\text{rows}}$  would be anti-conservative. The theorem-backed uniform-causal prediction gives zero floor violations; the optimizer location is reported as an empirical landscape statistic, not as a theoretical prediction. Empirical results are visualised in Fig. 3b; Flan-T5 decoder/TruthfulQA omitted because no samples passed the  $n \geq 32$  filter (very short T5 decoder responses on TruthfulQA prompts).

Model	Dataset	$n_{\text{rows}}$	$\langle t^*/n \rangle$	$\langle \min_t \hat{\phi} \rangle$	Viol. of 1/5
			(empirical)	(theory: $\phi \geq 0.20$ )	(95% clustered CI)
GPT-2	HaluEval	7200	$0.51 \pm 0.13$	$0.27 \pm 0.15$	$36\%_{35}^{38}$
GPT-2	MedHallu	7200	$0.50 \pm 0.11$	$0.25 \pm 0.15$	$42\%_{41}^{43}$
GPT-2	TruthfulQA	6480	$0.50 \pm 0.14$	$0.27 \pm 0.15$	$37\%_{36}^{38}$
Pythia-160M	HaluEval	7200	$0.67 \pm 0.27$	$0.18 \pm 0.14$	$65\%_{61}^{68}$
Pythia-160M	MedHallu	7200	$0.64 \pm 0.26$	$0.15 \pm 0.12$	$70\%_{68}^{71}$
Pythia-160M	TruthfulQA	6480	$0.52 \pm 0.21$	$0.22 \pm 0.18$	$55\%_{51}^{59}$
Flan-T5 dec.	HaluEval	5040	$0.50 \pm 0.22$	$0.12 \pm 0.10$	$79\%_{78}^{80}$
Flan-T5 dec.	MedHallu	2400	$0.48 \pm 0.20$	$0.10 \pm 0.10$	$82\%_{80}^{83}$

Metric	Purpose	Conf.	Assump.
Raw	Baseline discrim.	None	–
Resid.	Remove linear len.	Linear	Linear
Strat.	Within-bin discrim.	Nonpar.	Bins
LC	Strat. + within-bin resid.	Both	Bins + linear
Overlap	Balanced-bin	Nonpar.	Prev.

Table 4: **AUROC variants and their properties.** Conf.: confound addressed. Assump.: modeling assumptions.

Table 5: Length-controlled AUROC comparison: zero-shot transport features versus baselines. **Left of bar:** Our zero-shot features— $\hat{\phi}$  CVaR<sub>75</sub> (high conductance), CVaR<sub>25</sub> (low conductance);  $\sigma_2$  std (spectral variability). **Right of bar:** Baselines—LLM-Check (attn/hidden/logit probes) and EigenTrack (supervised). Values show AUROC with 95% bootstrap confidence intervals (super/subscript notation). **Bold** = best per row; this paper’s contribution is diagnostic characterization, not detection ranking. Per-row cell shading: green for the top two values (darker = higher), vermilion for the bottom two (darker = lower); tied values share a shade. All methods use length-controlled (within-bin residualized, pair-weighted) evaluation.  $G$  std (asymmetry) results appear in Figure 6.

Model	Dataset	Transport features (ours)			Baselines			
		$\hat{\phi}$ C <sub>75</sub>	$\hat{\phi}$ C <sub>25</sub>	$\sigma_2$ std	LLM <sub>attn</sub>	LLM <sub>hid</sub>	LLM <sub>log</sub>	ET
GPT-2	HaluEval	0.68 <sup>.71</sup> <sub>.66</sub>	0.55 <sup>.58</sup> <sub>.53</sub>	<b>0.77</b> <sup>.79</sup> <sub>.74</sub>	0.64 <sup>.75</sup> <sub>.57</sub>	0.71 <sup>.81</sup> <sub>.62</sub>	0.69 <sup>.81</sup> <sub>.62</sub>	0.63 <sup>.66</sup> <sub>.61</sub>
GPT-2	TruthfulQA	<b>0.61</b> <sup>.64</sup> <sub>.59</sub>	0.57 <sup>.59</sup> <sub>.54</sub>	0.60 <sup>.62</sup> <sub>.58</sub>	0.55 <sup>.63</sup> <sub>.53</sub>	<b>0.63</b> <sup>.71</sup> <sub>.58</sub>	0.58 <sup>.65</sup> <sub>.53</sub>	0.50 <sup>.50</sup> <sub>.50</sub>
GPT-2	MedHallu	0.58 <sup>.64</sup> <sub>.55</sub>	0.61 <sup>.66</sup> <sub>.57</sub>	0.55 <sup>.61</sup> <sub>.52</sub>	0.62 <sup>.69</sup> <sub>.57</sub>	<b>0.65</b> <sup>.71</sup> <sub>.59</sub>	0.64 <sup>.72</sup> <sub>.58</sub>	0.57 <sup>.64</sup> <sub>.54</sub>
BERT	HaluEval	0.57 <sup>.60</sup> <sub>.55</sub>	0.59 <sup>.62</sup> <sub>.56</sub>	0.55 <sup>.58</sup> <sub>.53</sub>	0.60 <sup>.79</sup> <sub>.59</sub>	<b>0.70</b> <sup>.83</sup> <sub>.59</sub>		0.62 <sup>.64</sup> <sub>.59</sub>
BERT	TruthfulQA	0.55 <sup>.58</sup> <sub>.53</sub>	0.56 <sup>.58</sup> <sub>.54</sub>	0.55 <sup>.58</sup> <sub>.53</sub>	0.57 <sup>.65</sup> <sub>.54</sub>	<b>0.62</b> <sup>.69</sup> <sub>.57</sub>		0.52 <sup>.56</sup> <sub>.51</sub>
BERT	MedHallu	0.58 <sup>.63</sup> <sub>.55</sub>	0.54 <sup>.60</sup> <sub>.52</sub>	0.63 <sup>.68</sup> <sub>.59</sub>	0.64 <sup>.71</sup> <sub>.59</sub>	<b>0.72</b> <sup>.78</sup> <sub>.64</sub>		0.54 <sup>.62</sup> <sub>.53</sub>
Pythia-160M	HaluEval	0.82 <sup>.84</sup> <sub>.80</sub>	0.62 <sup>.64</sup> <sub>.59</sub>	<b>0.84</b> <sup>.86</sup> <sub>.81</sub>	0.70 <sup>.82</sup> <sub>.62</sub>	0.72 <sup>.80</sup> <sub>.63</sub>	0.80 <sup>.89</sup> <sub>.59</sub>	0.60 <sup>.62</sup> <sub>.58</sub>
Pythia-160M	TruthfulQA	0.57 <sup>.59</sup> <sub>.55</sub>	0.58 <sup>.61</sup> <sub>.56</sub>	0.57 <sup>.60</sup> <sub>.55</sub>	0.52 <sup>.61</sup> <sub>.52</sub>	<b>0.63</b> <sup>.72</sup> <sub>.58</sub>	0.52 <sup>.60</sup> <sub>.52</sub>	0.52 <sup>.56</sup> <sub>.51</sub>
Pythia-160M	MedHallu	0.61 <sup>.67</sup> <sub>.58</sub>	<b>0.62</b> <sup>.68</sup> <sub>.58</sub>	0.59 <sup>.65</sup> <sub>.55</sub>	0.62 <sup>.69</sup> <sub>.57</sub>	0.62 <sup>.69</sup> <sub>.57</sub>	0.58 <sup>.65</sup> <sub>.54</sub>	0.61 <sup>.68</sup> <sub>.56</sub>
Flan-T5 (cross)	HaluEval	0.62 <sup>.64</sup> <sub>.59</sub>	<b>0.71</b> <sup>.73</sup> <sub>.68</sub>	0.66 <sup>.69</sup> <sub>.64</sub>	0.62 <sup>.74</sup> <sub>.55</sub>			0.50 <sup>.50</sup> <sub>.50</sub>
Flan-T5 (cross)	TruthfulQA	0.53 <sup>.56</sup> <sub>.52</sub>	0.58 <sup>.60</sup> <sub>.55</sub>	0.57 <sup>.60</sup> <sub>.55</sub>	<b>0.59</b> <sup>.67</sup> <sub>.55</sub>			0.53 <sup>.57</sup> <sub>.52</sub>
Flan-T5 (cross)	MedHallu	0.56 <sup>.61</sup> <sub>.53</sub>	0.67 <sup>.72</sup> <sub>.63</sub>	<b>0.68</b> <sup>.73</sup> <sub>.63</sub>	0.55 <sup>.64</sup> <sub>.53</sub>			0.50 <sup>.50</sup> <sub>.50</sub>
Flan-T5 (dec)	HaluEval	0.73 <sup>.75</sup> <sub>.71</sub>	0.73 <sup>.76</sup> <sub>.71</sub>	0.69 <sup>.72</sup> <sub>.67</sub>	<b>0.77</b> <sup>.85</sup> <sub>.69</sub>	0.72 <sup>.82</sup> <sub>.60</sub>	0.68 <sup>.80</sup> <sub>.61</sub>	0.50 <sup>.50</sup> <sub>.50</sub>
Flan-T5 (dec)	TruthfulQA	0.54 <sup>.58</sup> <sub>.53</sub>	0.55 <sup>.58</sup> <sub>.53</sub>	0.53 <sup>.56</sup> <sub>.51</sub>	<b>0.60</b> <sup>.67</sup> <sub>.57</sub>	0.59 <sup>.67</sup> <sub>.56</sub>	0.56 <sup>.64</sup> <sub>.53</sub>	0.53 <sup>.57</sup> <sub>.52</sub>
Flan-T5 (dec)	MedHallu	0.53 <sup>.58</sup> <sub>.52</sub>	0.57 <sup>.61</sup> <sub>.53</sub>	0.56 <sup>.61</sup> <sub>.53</sub>	0.59 <sup>.66</sup> <sub>.55</sub>	0.60 <sup>.67</sup> <sub>.55</sub>	<b>0.60</b> <sup>.69</sup> <sub>.56</sub>	0.50 <sup>.50</sup> <sub>.50</sub>

Table 6: **Feature-set ablation: does the asymmetry axis  $G$  add discriminative signal beyond the symmetric axis?** Length-controlled AUROC (LC-AUROC) with 95% bootstrap confidence intervals (super/subscript notation) of logistic-regression probes fit on z-scored feature sets via 5-fold cross-validation (out-of-fold scores; same supervised convention as the EigenTrack baseline), using the main-table aggregations ( $\hat{\phi}$  CVaR<sub>75</sub>,  $\hat{\phi}$  CVaR<sub>25</sub>,  $\sigma_2$  std,  $G$  std).  $\Delta$  is the paired difference (full minus symmetric);  $\Delta > 0$  means adding  $G$  improves discrimination, with a paired-bootstrap CI on the difference. **Bold  $\Delta$** : CI excludes zero in favor of  $G$ ; *italic  $\Delta$* : CI excludes zero against  $G$  (reversal). Llama-3.1-8B rows are the modern-model generalization check, not part of the main results grid.

Model	Data set	$n$	$\{\hat{\phi}, \sigma_2\}$	$\{\hat{\phi}, \sigma_2, G\}$	$\{G\}$	$\Delta$ (full - sym)
GPT-2	HaluEval	5904	0.750 <sup>.780</sup> <sub>.726</sub>	0.750 <sup>.779</sup> <sub>.725</sub>	0.627 <sup>.656</sup> <sub>.603</sub>	-0.000 <sup>+.005</sup> <sub>-.006</sub>
	TruthfulQA	1963	0.594 <sup>.621</sup> <sub>.572</sub>	0.604 <sup>.631</sup> <sub>.580</sub>	0.581 <sup>.606</sup> <sub>.558</sub>	+0.010 <sup>+.021</sup> <sub>-.002</sub>
	MedHallu	618	0.588 <sup>.642</sup> <sub>.549</sub>	0.521 <sup>.588</sup> <sub>.519</sub>	0.609 <sup>.658</sup> <sub>.562</sub>	-0.068 <sup>+.012</sup> <sub>-.094</sub>
Pythia	HaluEval	5904	0.828 <sup>.856</sup> <sub>.802</sub>	0.837 <sup>.864</sup> <sub>.813</sub>	0.816 <sup>.841</sup> <sub>.790</sub>	<b>+0.009</b> <sup>+.016</sup> <sub>+.002</sub>
	TruthfulQA	1963	0.543 <sup>.570</sup> <sub>.527</sub>	0.587 <sup>.611</sup> <sub>.562</sub>	0.594 <sup>.621</sup> <sub>.572</sub>	<b>+0.044</b> <sup>+.066</sup> <sub>+.013</sub>
	MedHallu	618	0.530 <sup>.593</sup> <sub>.519</sub>	0.618 <sup>.672</sup> <sub>.578</sub>	0.605 <sup>.661</sup> <sub>.571</sub>	<b>+0.089</b> <sup>+.126</sup> <sub>+.013</sub>
BERT	HaluEval	5904	0.547 <sup>.581</sup> <sub>.527</sub>	0.569 <sup>.600</sup> <sub>.542</sub>	0.578 <sup>.608</sup> <sub>.552</sub>	+0.022 <sup>+.061</sup> <sub>-.028</sub>
	TruthfulQA	1963	0.538 <sup>.565</sup> <sub>.522</sub>	0.581 <sup>.608</sup> <sub>.558</sub>	0.592 <sup>.618</sup> <sub>.571</sub>	<b>+0.044</b> <sup>+.067</sup> <sub>+.011</sub>
	MedHallu	618	0.566 <sup>.624</sup> <sub>.539</sub>	0.576 <sup>.633</sup> <sub>.544</sub>	0.592 <sup>.645</sup> <sub>.557</sub>	+0.010 <sup>+.024</sup> <sub>-.011</sub>
Flan-T5 (cross)	HaluEval	5904	0.723 <sup>.748</sup> <sub>.696</sub>	0.722 <sup>.748</sup> <sub>.695</sub>	0.535 <sup>.565</sup> <sub>.521</sub>	-0.001 <sup>+.004</sup> <sub>-.004</sub>
	TruthfulQA	1951	0.538 <sup>.566</sup> <sub>.520</sub>	0.562 <sup>.588</sup> <sub>.540</sub>	0.525 <sup>.557</sup> <sub>.517</sub>	<b>+0.024</b> <sup>+.048</sup> <sub>+.000</sub>
	MedHallu	618	0.679 <sup>.724</sup> <sub>.630</sub>	0.686 <sup>.730</sup> <sub>.636</sub>	0.581 <sup>.640</sup> <sub>.549</sub>	+0.007 <sup>+.020</sup> <sub>-.005</sub>
Flan-T5 (dec)	HaluEval	5904	0.768 <sup>.793</sup> <sub>.745</sub>	0.756 <sup>.781</sup> <sub>.731</sub>	0.779 <sup>.800</sup> <sub>.756</sub>	<i>-0.012</i> <sup>-.008</sup> <sub>-.017</sub>
	TruthfulQA	1951	0.550 <sup>.578</sup> <sub>.531</sub>	0.562 <sup>.590</sup> <sub>.538</sub>	0.563 <sup>.590</sup> <sub>.537</sub>	+0.012 <sup>+.031</sup> <sub>-.011</sub>
	MedHallu	618	0.546 <sup>.598</sup> <sub>.526</sub>	0.541 <sup>.592</sup> <sub>.523</sub>	0.582 <sup>.635</sup> <sub>.551</sub>	-0.005 <sup>+.027</sup> <sub>-.035</sub>
Llama-3.1-8B	HaluEval	5904	0.721 <sup>.747</sup> <sub>.696</sub>	0.745 <sup>.770</sup> <sub>.721</sub>	0.539 <sup>.566</sup> <sub>.521</sub>	<b>+0.025</b> <sup>+.034</sup> <sub>+.014</sub>
	TruthfulQA	1963	0.609 <sup>.635</sup> <sub>.585</sub>	0.608 <sup>.635</sup> <sub>.584</sub>	0.541 <sup>.567</sup> <sub>.525</sub>	-0.001 <sup>+.006</sup> <sub>-.008</sub>
	MedHallu	618	0.547 <sup>.606</sup> <sub>.530</sub>	0.538 <sup>.595</sup> <sub>.524</sub>	0.588 <sup>.640</sup> <sub>.546</sub>	-0.009 <sup>+.019</sup> <sub>-.037</sub>

Table 7: **Cross-architecture generalization to a modern model.** Flipped length-controlled AUROC (LC-AUROC) of the transport diagnostics on LLaMA-3.1-8B (decoder-only, grouped-query attention, RoPE), with 95% bootstrap confidence intervals (super/subscript notation). LLaMA was extracted with the same spectral-sweep conductance estimator as the main results; baselines were not evaluated on this model, so only transport diagnostics are reported. The capacity axis ( $\hat{\phi}, \sigma_2$ ) retains signal at 8B scale, while the asymmetry axis  $G$  stays near chance, consistent with the main results.

Data set	$\hat{\phi}$ CVaR <sub>75</sub>	$\sigma_2$ std	$G$ std
HaluEval ( $n=5904$ )	0.664 <sup>.689</sup> <sub>.641</sub>	0.717 <sup>.742</sup> <sub>.694</sub>	0.542 <sup>.568</sup> <sub>.524</sub>
TruthfulQA ( $n=1963$ )	0.608 <sup>.633</sup> <sub>.582</sub>	0.581 <sup>.607</sup> <sub>.557</sub>	0.551 <sup>.578</sup> <sub>.530</sub>
MedHallu ( $n=618$ )	0.603 <sup>.658</sup> <sub>.563</sub>	0.554 <sup>.607</sup> <sub>.528</sub>	0.589 <sup>.639</sup> <sub>.546</sub>

**Roadmap.** This appendix collects the longer proofs behind the paper’s headline structural results. The orientation-blindness theorem and its Lipschitz converse (Theorem 5, Theorem 8) and the dilation-spectrum lemma (Theorem 2) are stated and proved in place in the main text. Appendix B gives the two-sided conductance bounds with the  $n$ -independent  $1/5$  floor, the causal asymmetry-energy and quantitative  $G$  bounds, and a restatement of degree sufficiency; Appendix C proves the asymmetry-coefficient characterization (Theorem 9:  $G = 0$  iff symmetric, the causal  $G \leq 1/\sqrt{2}$  ceiling, and the encoder/decoder distinction). Only the supporting lemmas for the architecture-specific quantitative  $G$ -bounds (softmax order preservation and the Toeplitz–Frobenius identity) remain in the Online Supplement (§17). The Reproducibility Statement (Appendix A) documents code, data provenance, and compute.

**Online Supplement (a separate companion document).** The Online Supplement collects the extended empirical material that *supports* the main argument but is not needed to follow it; the main text references it once per topic rather than per claim. It contains: detailed AUROC tables and per-quartile breakdowns (§§1,4); complementary diagnostics (§2); the length-confounding analysis and the per-method derivations for LLM-Check, EigenTrack, and LapEigvals (§§3,6–8); dataset statistics (§5); LC-AUROC sensitivity (§9); finite-size and random-matrix analysis (§10); the degree-sufficiency and matched-null validations (§§11,15); alternative  $G$ -norms (§12); supplementary figures (§13); the bipartite-SVD analysis underlying the Hermitian dilation (§14); evaluation-metric definitions (§16); and supporting cross-attention proofs (§17).

## A Reproducibility

**Data provenance.** HaluEval ( $n=10,000$ , HuggingFace pminervini/HaluEval); TruthfulQA ( $n=817$ , truthfulqa/truthful\_qa); MedHallu ( $n=1,000$ , UTHealth/MedHallu). Pre-processing is deterministic via hash-based splitting.

**Model checkpoints.** All models are publicly available on HuggingFace: GPT-2, Pythia-160M, BERT-base-uncased, Flan-T5-base, and LLaMA-3.1-8B (cross-architecture generalization check).

**Compute environment.** Experiments were run on a single NVIDIA A10G GPU (24 GB GDDR6) with 16 vCPUs (AMD EPYC 7R32) and 64 GiB system RAM. A single GPU is sufficient for the full experiment suite at the model scales reported. Software dependencies are pinned (Python 3.11, PyTorch 2.1, Transformers 4.36). Random seeds are fixed per experiment configuration.

**Formal verification.** A Lean 4 formalization of the core structural lemmas accompanies the paper; it is `sorry`-free and uses no custom axioms.

## B Structural Regime Propositions and Proofs

This appendix contains the proofs of the headline theorems cited in the main text: the two-sided diagnostic theorem (Sec. B.2.3) and the asymmetry-energy proposition (Sec. B.3.1); the asymmetry-coefficient characterization ( $G = 0$  iff symmetric, the causal  $1/\sqrt{2}$  ceiling, and the encoder–decoder distinction) is proved in Appendix C. The supporting cross-attention analysis ( $n_q \neq n_k$ , relevant only to encoder–decoder architectures), the foundational concentration lemmas, and the architecture-dependent quantitative  $G$  bounds are in the

Online Supplement (§17); decoder-only results in the main text do not depend on that material.

## B.1 Proposition Statements

**Proposition 15 (Degree imbalance induces length entanglement of  $\sigma_2$ )** In cross-attention regimes: Assume  $\mathbf{B}$  is row-stochastic and each query distributes mass approximately uniformly over an effective support of size  $s$ . As  $n_q$  increases with  $n_k$  fixed (regime  $n_q \gg n_k$ ), the spectrum of  $\mathcal{M}$  (and in particular  $\sigma_2(\mathcal{M})$ ) becomes strongly entangled with generation length through column normalization.

**Theorem 4** (Conductance bounds both failure modes). See Sec. 3 for the main statement. The detailed proof with explicit conductance bounds appears in Sec. B.2.3.

**Proposition 11** (Causal attention implies  $G > 0$ ). See Sec. 5 for the statement; proof follows in Sec. B.3.1.

**Theorem 3** (Degree sufficiency for near-regular attention). See Sec. 3 for the full statement and proof.

*Conductance transfer corollary.* The Cheeger bridge inequality  $\delta/2 \leq \phi \leq \sqrt{2\delta}$  (where  $\delta = 1 - \sigma_2$ ) transfers the spectral perturbation to conductance. If the spectral gaps of  $\mathcal{M}$  and  $A/\sqrt{d}$  differ by at most  $\varepsilon = \max_j |1 - \sqrt{d_j/d}| (\leq \sqrt{\kappa} - 1)$ , then for the upper Cheeger bound  $\phi(\mathcal{M}) \leq \sqrt{2\delta_{\mathcal{M}}}$  and the lower bound  $\delta_{\text{ref}}/2 \leq \phi_{\text{ref}}$ , the conductance perturbation satisfies

$$\phi(\mathcal{M}) - \phi_{\text{ref}} \leq \sqrt{2(\delta_{\text{ref}} + \varepsilon)} - \delta_{\text{ref}}/2.$$

For small  $\varepsilon$ , this is  $O(\sqrt{\varepsilon})$ .

The remainder of the structural-regime analysis (the foundational technical lemmas ( $D_K$ -scaling and degree-balance), the proof of Theorem 15, the degree-ratio Cheeger bound, the diffuse-key regime ( $n_k \gg n_q$ ) analysis, the positional-encoding quantitative  $G$  bounds, and the empirical polarity analysis) is deferred to the Online Supplement (§17).

## B.2 Conductance Bounds and Proofs

This section establishes conductance bounds for causal attention patterns, including the window attention bottleneck bound and uniform causal conductance lower bound that support Theorem 4.

### B.2.1 Window Attention Conductance Bound

**Lemma 16 (Window attention conductance bound)** For  $w$ -window causal attention  $\mathbf{B}_{ij} = (1/\min(w, i+1))\mathbf{1}\{\max(0, i-w+1) \leq j \leq i\}$  and any nontrivial temporal bipartite cut  $S_t$  with  $0 < t < n$ :

$$\phi(S_t) \leq \frac{w}{\min(t, n-t)}.$$

In particular, for late-half cuts satisfying  $n-t \leq t$ ,  $\phi(S_t) \leq w/(n-t)$ .

**Proof.** Only queries  $i \in [t, t+w-1]$  can contribute to the cut (by window structure). Each contributes at most mass 1 (row-stochastic), so  $\text{cut}(S_t) \leq w$ . The query side contributes volume at least  $t$ , and the query-side complement contributes volume at least  $n-t$ ; hence the Cheeger denominator is at least  $\min(t, n-t)$ . If  $n-t \leq t$ , this specializes to the denominator  $n-t$ .  $\square$

### B.2.2 Uniform Causal Conductance: Cut, Volume, and Conductance Identities

We work in the symmetric bipartite graph  $\mathcal{H}(\mathbf{B})$  with vertex set  $\{Q_0, \dots, Q_{n-1}\} \cup \{K_0, \dots, K_{n-1}\}$  and edge weights  $W_{Q_i K_j} = \mathbf{B}_{ij}$ . The temporal cut  $S_t = \{Q_0, \dots, Q_{t-1}\} \cup \{K_0, \dots, K_{t-1}\}$  partitions vertices by index. The following three propositions establish the closed-form arithmetic of conductance on this cut family for uniform causal attention; the lemma cited by the two-sided diagnostic is then a one-line corollary.

**Proposition 17 (Cut and volume identities for uniform causal attention)** *For uniform causal attention  $\mathbf{B}_{ij} = (1/(i+1)) \mathbf{1}\{j \leq i\}$  and the temporal cut  $S_t$  with  $0 \leq t \leq n$ :*

$$\text{cut}(S_t) = t(H_n - H_t), \quad \text{vol}(S_t) = t(2 + H_n - H_t). \quad (8)$$

**Proof.** The causal mask forces only  $(Q_i, K_j)$  with  $i \geq t, j < t$  to cross the cut, so  $\text{cut}(S_t) = \sum_{i=t}^{n-1} \sum_{j=0}^{t-1} 1/(i+1) = t(H_n - H_t)$ . Vertex weights on the dilation graph are  $W(Q_i) = \sum_j \mathbf{B}_{ij} = 1$  (row-stochasticity) and  $W(K_j) = \sum_i \mathbf{B}_{ij} = H_n - H_j$  (column sum). The volume of  $S_t$  is  $\sum_{i < t} 1 + \sum_{j < t} (H_n - H_j)$ ; applying the harmonic-of-harmonic identity  $\sum_{j=0}^{t-1} H_j = tH_t - t$  [Graham et al., 1994, Eq. (6.69)] gives  $\text{vol}(S_t) = t + tH_n - (tH_t - t) = t(2 + H_n - H_t)$ .  $\square$

**Proposition 18 (Total volume of the bipartite dilation graph)** *For any non-negative row-stochastic matrix  $\mathbf{B} \in \mathbb{R}^{n \times n}$ , the total volume of its bipartite dilation graph  $\mathcal{H}(\mathbf{B})$  equals  $2n$ . Consequently, for any cut  $S$  on the dilation graph,  $\min(\text{vol}(S), \text{vol}(\bar{S})) \leq n$ .*

**Proof.** The total volume is  $\sum_{i=0}^{n-1} W(Q_i) + \sum_{j=0}^{n-1} W(K_j) = \sum_i \sum_j \mathbf{B}_{ij} + \sum_j \sum_i \mathbf{B}_{ij} = 2 \sum_{i,j} \mathbf{B}_{ij} = 2n$ , using row-stochasticity. The min bound follows since  $\text{vol}(S) + \text{vol}(\bar{S}) = 2n$ .  $\square$

**Proof structure (closed-form landscape).**

**Foundations.** Harmonic-number inequality  $H_n - H_{\lfloor n/2 \rfloor} \geq 1/2$  [Graham et al., 1994, Eq. (6.69)]; the bipartite Cheeger conductance definition  $\phi(S) = \text{cut}(S) / \min(\text{vol}(S), \text{vol}(\bar{S}))$ .

**Bridge.** Bipartite dilation  $\mathcal{H}(\mathbf{B})$  as the symmetric graph carrying the asymmetric attention pattern (Theorem 18); cut and volume identities  $\text{cut}(S_t) = t(H_n - H_t)$ ,  $\text{vol}(S_t) = t(2 + H_n - H_t)$  (Theorem 17).

**Contribution.** The closed-form functional  $\phi(S_t) \geq u(t)/(2 + u(t))$  (Theorem 19) and its  $n$ -independent floor  $\phi \geq 1/5$  for every  $n \geq 2$  (Theorem 20). This is the architectural benchmark against which the empirical landscape signature is read: real attention heads piercing  $1/5$  on HaluEval form the population fraction (Table 3) that distinguishes position-encoding regimes. Together with the window-attention bottleneck (Theorem 16), it delivers the polarity reversal of the two-sided diagnostic (Theorem 4).

**Lemma 19 (Uniform causal conductance, functional form)** *For uniform causal attention and any temporal cut  $0 < t < n$ , writing  $u(t) = H_n - H_t$ ,*

$$\phi(S_t) \geq \frac{u(t)}{2 + u(t)}. \quad (9)$$

*This bound is uniform: it holds in both the small-side regime ( $\text{vol}(S_t) \leq \text{vol}(\bar{S}_t)$ , where it is achieved with equality) and the large-side regime (where it is strict).*

**Proof.** By definition  $\phi(S_t) = \text{cut}(S_t) / \min(\text{vol}(S_t), \text{vol}(\bar{S}_t))$ . Theorem 17 gives  $\text{cut}(S_t) = t u$  and  $\text{vol}(S_t) = t(2 + u)$ . Since  $\min(\text{vol}(S_t), \text{vol}(\bar{S}_t)) \leq \text{vol}(S_t)$ ,

$$\phi(S_t) \geq \frac{\text{cut}(S_t)}{\text{vol}(S_t)} = \frac{t u}{t(2 + u)} = \frac{u}{2 + u}.$$

In the small-side regime,  $\min = \text{vol}(S_t)$  and the inequality is equality; in the large-side regime,  $\min = \text{vol}(\bar{S}_t) < \text{vol}(S_t)$ , so dividing by the smaller denominator gives strict inequality.  $\square$

Theorem 19 characterises conductance as a monotone function of the harmonic-mass-above- $t$  parameter  $u = H_n - H_t$ . Two corollaries record the numerical consequences.

**Corollary 20 ( $n$ -independent conductance lower bound)** *For uniform causal attention and any  $0 < t < n$  with  $n \geq 2$ ,*

$$\phi(S_t) \geq \frac{1}{5}.$$

**Proof.** The proof is by a two-branch split on the volume ordering. If  $\text{vol}(S_t) \leq \text{vol}(\bar{S}_t)$ , then the volume identity (8) forces  $2t \leq n$ . Hence  $t \leq \lfloor n/2 \rfloor$  and

$$u(t) = H_n - H_t \geq H_n - H_{\lfloor n/2 \rfloor} \geq \frac{1}{2},$$

where the last inequality is the elementary harmonic-tail bound that the sum has at least  $\lfloor n/2 \rfloor$  terms, each at least  $1/n$ . The small-side formula therefore gives  $\phi(S_t) \geq u(t)/(2 + u(t)) \geq 1/5$ .

If instead  $\text{vol}(\bar{S}_t) \leq \text{vol}(S_t)$ , then

$$\phi(S_t) = \frac{t u(t)}{2n - t(2 + u(t))}.$$

For  $2t \leq n$  the same harmonic-tail bound gives  $u(t) \geq 1/2$ ; for  $n < 2t$  the lower tail estimate  $H_n - H_t \geq (n - t)/n$  gives the required denominator comparison  $2n - t(2 + u(t)) \leq 5t u(t)$ . In both subcases  $\phi(S_t) \geq 1/5$ .  $\square$

**Corollary 21 (Asymptotic conductance bound)** *For any  $n \geq 2$  and  $0 < t < n$ ,*

$$\phi(S_t) \geq \frac{1}{2 \log n + 2}. \quad (10)$$

**Proof.** Theorem 20 gives the stronger bound  $1/5$  whenever  $1/5 \geq 1/(2 \log n + 2)$ , i.e.,  $n \geq e^{3/2} > 4$ . Direct enumeration covers  $n \in \{2, 3, 4\}$  via (8):  $\phi_{\min} = 1/3, 5/17, 13/37$  at  $n = 2, 3, 4$  respectively, each exceeding  $1/(2 \log n + 2) \approx 0.295, 0.238, 0.209$ .  $\square$

**Remark 22 (Why this is not just an instance of Cheeger)** *The classical Cheeger inequality (3) is a bidirectional bridge between conductance and the spectral gap:  $\phi^2/2 \leq 1 - \sigma_2 \leq 2\phi$ . It does not, by itself, deliver a numerical lower bound on  $\phi$  for any specific operator – using it in that direction requires an independent estimate of  $\sigma_2$ . The identities and bound above provide structure that classical Cheeger alone does not supply.*

*First, Theorem 17 delivers cut and vol as exact equalities, not bounds; these are bookkeeping facts about the matrix structure that Cheeger has no reason to know. Second, Theorem 19 gives a closed-form functional bound  $\phi(S_t) \geq u(t)/(2 + u(t))$  – characterising how conductance varies with cut location, not just its minimum. Third, the volume-crossover branch is localised by the formal halfway theorem: if  $S_t$  is the small side then  $2t \leq n$ , and after halfway the complement is the small side. Fourth, the constant  $\phi \geq 1/5$  in Theorem 20 is  $n$ -independent, strictly sharper than what Cheeger composed with any  $\sigma_2$  estimate of  $O(1/\sqrt{n})$ -type would give for moderate  $n$ . The architectural consequence is what the two-sided diagnostic (Theorem 4) needs: uniform causal attention has positive conductance as a structural fact about its causal mask, not as a conditional fact about its spectrum.*

The proof technique generalises: the row-sum / column-sum decomposition of the bipartite-dilation cut and volume (Theorems 17 and 18) is the same template for any causal architecture (window, exponential decay, RoPE-style monotone mass). Each architecture produces its own closed form for  $\text{cut}(S_t)$  and  $\text{vol}(S_t)$ ; the resulting conductance bound follows by the same one-line argument as in Theorem 19.

**Remark 23 (Asymptotic conductance landscape)** A more careful optimizer analysis can be carried out from the same closed-form landscape, but it is not needed for the theorem-backed floor. The closed form yields the cut/volume identities, the functional lower bound, the  $1/5$  floor, and the halfway localization of the volume-crossover branch; a sharp discrete optimizer location is not established here.

**Remark 24 (Conductance landscape of uniform causal attention)** Theorem 19 delivers more than a uniform floor: it characterises the entire conductance landscape as a function of cut location. Writing  $u(t) = H_n - H_t$ , conductance varies from  $\approx H_n - 1 \approx \log n$  at  $t = 1$  (early cut, harmonic mass mostly above), through a localised crossover candidate, back up to  $\approx 1$  at  $t = n - 1$  (late cut, vanishing remaining mass). The diagnostic implication is that uniform causal attention has a localised bottleneck candidate, with conductance behaving smoothly on either side. This contrasts with  $w$ -window attention (Theorem 16), where balanced temporal cuts have  $\phi = O(w/n)$  and the bottleneck is global rather than localised.

### B.2.3 Proof of Two-Sided Diagnostic Theorem

**Statement (restated).** In square, causally masked attention ( $n_q = n_k = n$  with lower-triangular support), incorrect behavior can arise from (i) concentration on a narrow temporal band (bottleneck) yielding  $\hat{\phi} \downarrow$ , or (ii) coherent but misguided routing over a broad temporal region yielding  $\hat{\phi}$  moderate/high. Therefore  $\hat{\phi}$  does not admit a universal polarity with correctness in decoder self-attention.

**Proof structure.**

**Foundations.** The bipartite Cheeger conductance  $\phi(S) = \text{cut}(S) / \min(\text{vol}(S), \text{vol}(\bar{S}))$  on the symmetric dilation graph  $\mathcal{H}(\mathbf{B})$ .

**Bridge.** Two canonical causal families serving as failure-mode prototypes:  $w$ -window attention (Theorem 16) and uniform causal attention (Theorems 17, 19 and 20); the temporal cut  $S_t$  as the index-aligned partition revealing routing behaviour at every position.

**Contribution.** Both families satisfy the same causal mask, yet their conductance landscapes are qualitatively opposite: window attention pierces the Cheeger floor uniformly ( $\phi \rightarrow 0$ ), while uniform causal attention respects an  $n$ -independent floor  $\phi \geq 1/5$ . Polarity of  $\hat{\phi}$  with respect to correctness therefore cannot be universal in decoder self-attention; it is determined by which failure-mode prototype dominates, not by task semantics. This is the structural reason the empirical polarity reverses across HaluEval (bottleneck-dominated) and MedHallu (diffuse-dominated).

**Proof.** We establish quantitative bounds for two canonical causal attention families, both satisfying the causal constraint  $\mathbf{B}_{ij} = 0$  for  $j > i$ .

(i) **Bottleneck family (Lemma 16).** Let  $\mathbf{B}$  be  $w$ -window causal attention:

$$\mathbf{B}_{ij} = \frac{1}{\min(w, i+1)} \mathbf{1}\{\max(0, i-w+1) \leq j \leq i\}.$$

For the temporal cut  $S_t = \{k_0, \dots, k_{t-1}\}$  separating early from late keys:

- Only queries  $i \in [t, t+w-1]$  have windows crossing the cut boundary
- Each such query contributes at most mass 1 (row-stochastic)

- Total cut weight:  $\text{cut}(S_t) \leq w$
- The Cheeger denominator is at least  $\min(t, n - t)$

Thus the conductance satisfies:

$$\phi(S_t) \leq \frac{w}{\min(t, n - t)}.$$

For late-half cuts  $n - t \leq t$ , this becomes  $\phi(S_t) \leq w/(n - t)$ ; choosing balanced cuts gives  $O(w/n)$ .

(ii) **Diffuse family (Theorems 17, 19 and 20).** Let  $\mathbf{B}$  be uniform causal attention:

$$\mathbf{B}_{ij} = \frac{1}{i + 1} \mathbf{1}\{j \leq i\}.$$

Theorem 17 delivers the closed-form  $\text{cut}(S_t) = t(H_n - H_t)$  and  $\text{vol}(S_t) = t(2 + H_n - H_t)$ . Theorem 19 composes these into the functional bound  $\phi(S_t) \geq u(t)/(2 + u(t))$  where  $u(t) = H_n - H_t$ . Theorem 20 uses the formal small-side/large-side split and harmonic-tail lower bounds to yield the  $n$ -independent constant

$$\phi(S_t) \geq \frac{1}{5} > 0 \quad \text{for all } 0 < t < n, n \geq 2.$$

Both families satisfy the same causal constraint but exhibit opposite conductance behaviour. The bottleneck family pierces the Cheeger floor on balanced cuts, while the diffuse family has  $\phi(S_t) \geq 1/5$  on *every* cut. For such balanced cuts,

$$\frac{\phi_{\text{uniform}}}{\phi_{\text{window}}} \geq \frac{\min(t, n - t)}{5w} \rightarrow \infty \quad \text{as } w/n \rightarrow 0$$

whenever  $\phi_{\text{window}} > 0$ ; if  $\phi_{\text{window}} = 0$ , the separation is even stronger. This establishes that  $\hat{\phi}$  does not admit a universal polarity in decoder self-attention: the conductance value depends on the attention *pattern* within the causal mask, not on task correctness.  $\square$

The Online Supplement (§13.1) illustrates how decoder self-attention mixes multiple failure modes, explaining polarity instability.

## B.3 Proofs: Asymmetric Transport

### B.3.1 Proof of Asymmetry Energy Proposition

**Statement (restated).** Let  $\mathcal{M}_{\text{asym}} = \frac{1}{2}(\mathcal{M} - \mathcal{M}^\top)$  and  $G = \|\mathcal{M}_{\text{asym}}\|_F / (\|\mathcal{M}\|_F + \varepsilon)$ . In square causal regimes,  $G$  decreases when transport becomes effectively reversible (forward/backward cancellation after normalization), even if conductance remains moderate.

**Proof structure.**

**Foundations.** Orthogonality of the symmetric and antisymmetric subspaces under the Frobenius inner product, yielding the Pythagorean identity  $\|\mathcal{M}\|_F^2 = \|\mathcal{M}_{\text{sym}}\|_F^2 + \|\mathcal{M}_{\text{asym}}\|_F^2$ .

**Bridge.** Definition of  $G(\mathcal{M}, \varepsilon) = \|\mathcal{M}_{\text{asym}}\|_F / (\|\mathcal{M}\|_F + \varepsilon)$  as the antisymmetric-residual norm (Sec. 5); restriction to square regimes ( $n_q = n_k$ ) where the symmetric-antisymmetric decomposition is well-posed.

**Contribution.**  $G$  is monotone non-increasing under symmetrisation of  $\mathcal{M}$  and detects orientation collapse that conductance cannot see:  $\hat{\phi}$  can remain moderate while  $G \downarrow$ , because conductance depends on cut capacity (a symmetric notion) rather than on irreversibility. This is the converse statement to orientation-blindness: *symmetric methods cannot detect orientation; G can.*

**Proof.** By definition,

$$G = \frac{\|\mathcal{M} - \mathcal{M}^\top\|_F}{2(\|\mathcal{M}\|_F + \varepsilon)}.$$

Thus  $G = 0$  if and only if  $\mathcal{M}$  is symmetric. More generally, if  $\mathcal{M}$  admits a decomposition

$$\mathcal{M} = S + R, \quad S^\top = S, \quad R^\top = -R,$$

then  $\mathcal{M}_{\text{asym}} = R$  and  $\|\mathcal{M}\|_F^2 = \|S\|_F^2 + \|R\|_F^2$  (orthogonality of symmetric and skew parts under Frobenius inner product). Hence

$$G = \frac{\|R\|_F}{\sqrt{\|S\|_F^2 + \|R\|_F^2 + \varepsilon}}.$$

If transport becomes more reversible in the sense that  $\|R\|_F$  decreases while  $\|S\|_F$  stays bounded away from zero, then  $G$  decreases. This can occur without inducing a bottleneck (i.e., without reducing conductance), because conductance depends primarily on cut capacity (a symmetric notion) rather than on irreversibility.

**Link to symmetric limitation.** By Theorem 5, any symmetric embedding derived from  $H(\mathcal{M})$  is invariant to transposition and therefore cannot encode irreversibility. Thus  $\hat{\phi}$  can remain moderate while  $G$  decreases, motivating  $G$  as a complementary axis.  $\square$

**Domain restriction (square matrices only).** The asymmetry energy  $G = \|\mathcal{M} - \mathcal{M}^\top\|_F / (2\|\mathcal{M}\|_F + \varepsilon)$  is defined only when  $\mathcal{M}$  is square ( $n_q = n_k$ ). In cross-attention with  $n_q \neq n_k$ , the difference  $\mathcal{M} - \mathcal{M}^\top$  is undefined because the transpose  $\mathcal{M}^\top \in \mathbb{R}^{n_k \times n_q}$  has different dimensions than  $\mathcal{M} \in \mathbb{R}^{n_q \times n_k}$ . Therefore,  $G$  applies exclusively to:

1. **Decoder self-attention:** inherently square due to causal masking ( $n_q = n_k = n$  at each position).
2. **Encoder self-attention:** square by construction (queries and keys from the same sequence).

For non-square cross-attention matrices, orientation diagnostics require alternative measures such as comparing the left and right singular vectors of  $\mathcal{M}$  directly, rather than relying on the symmetric–antisymmetric decomposition.

The Online Supplement (§13.2) illustrates how  $G$  captures orientation failures that  $\hat{\phi}$  misses due to its symmetry.

### B.3.2 Encoder vs Decoder: Structural vs Learned Asymmetry

The proposition above applies to “square, causal regimes,” but causal masking is only present in decoder self-attention. We now formalize the distinction between encoder and decoder attention with respect to  $G$ .

**Lemma 25 (Causal masking guarantees asymmetry)** *Let  $\mathbf{B}$  be a causal attention matrix (lower-triangular:  $\mathbf{B}_{ij} = 0$  for  $j > i$ ) with at least one positive off-diagonal entry  $\mathbf{B}_{i_0, j_0} > 0$  for some  $i_0 > j_0$ . Then the normalized operator  $\mathcal{M}$  satisfies  $\mathcal{M} \neq \mathcal{M}^\top$ , and consequently  $G > 0$  for any  $\varepsilon > 0$ .*

**Proof.** By assumption, there exists  $(i_0, j_0)$  with  $i_0 > j_0$  and  $\mathbf{B}_{i_0, j_0} > 0$ . Since  $D_Q(i_0) > 0$  and  $D_K(j_0) > 0$  (the row sum and column sum are positive),

$$\mathcal{M}_{i_0, j_0} = D_Q(i_0)^{-1/2} \mathbf{B}_{i_0, j_0} D_K(j_0)^{-1/2} > 0.$$

However, the causal constraint forces  $\mathbf{B}_{j_0, i_0} = 0$  (since  $j_0 < i_0$ ), hence  $\mathcal{M}_{j_0, i_0} = 0$ . Therefore  $\mathcal{M}_{i_0, j_0} \neq \mathcal{M}_{j_0, i_0}$ , which implies  $\mathcal{M} \neq \mathcal{M}^\top$ .

Since  $\mathcal{M} \neq \mathcal{M}^\top$ , we have  $\mathcal{M}_{\text{asym}} = \frac{1}{2}(\mathcal{M} - \mathcal{M}^\top) \neq 0$ , and thus

$$G = \frac{\|\mathcal{M}_{\text{asym}}\|_F}{\|\mathcal{M}\|_F + \varepsilon} > 0.$$

□

**Lemma 26 (Bidirectional attention admits symmetric solutions)** *For bidirectional self-attention (no causal mask), if the attention pattern is symmetric ( $\mathbf{B}_{ij} = \mathbf{B}_{ji}$  for all  $i, j$ ), then  $\mathcal{M} = \mathcal{M}^\top$  and  $G = 0$ .*

**Proof.** If  $\mathbf{B} = \mathbf{B}^\top$ , then the row sums equal the column sums:  $D_Q = D_K$ . Therefore:

$$\begin{aligned} \mathcal{M}_{ij} &= D_Q(i)^{-1/2} \mathbf{B}_{ij} D_K(j)^{-1/2}, \\ \mathcal{M}_{ji} &= D_Q(j)^{-1/2} \mathbf{B}_{ji} D_K(i)^{-1/2} \\ &= D_K(j)^{-1/2} \mathbf{B}_{ij} D_Q(i)^{-1/2} \\ &\quad (\text{using } \mathbf{B}_{ji} = \mathbf{B}_{ij}, D_Q = D_K) \\ &= \mathcal{M}_{ij}. \end{aligned}$$

Hence  $\mathcal{M} = \mathcal{M}^\top$ , so  $\mathcal{M}_{\text{asym}} = 0$  and  $G = 0$ . □

**Corollary 27 (Differential diagnostic interpretation)** *The guessing coefficient  $G$  has different diagnostic interpretations for encoder versus decoder attention:*

1. **Decoder self-attention:** *Causal masking structurally guarantees  $G > 0$  for any non-trivial attention pattern. When  $G$  decreases toward zero, the model’s forward and backward transport flows are canceling after degree normalization, an orientation collapse that indicates pathological behavior.*
2. **Encoder self-attention:** *No causal constraint exists, so  $G = 0$  is achievable in principle (symmetric attention patterns). Low  $G$  does not inherently indicate pathology; it may simply reflect learned symmetric routing.*

### B.3.3 Quantitative Bounds on $G$ for Causal Attention

We derive explicit bounds on  $G$  for canonical attention patterns to supplement the architecture-dependent interpretation in Sec. 5.

**Observation 28 ( $G$  for uniform causal attention: numerical limit)** *Let  $\mathbf{B}_{ij} = \frac{1}{i} \mathbf{1}\{j \leq i\}$  be uniform causal attention on  $n$  tokens, and let  $\mathcal{M} = D_Q^{-1/2} \mathbf{B} D_K^{-1/2}$  be its degree-normalised operator. Direct numerical evaluation gives  $G(\mathcal{M}) = \|\mathcal{M} - \mathcal{M}^\top\|_F / (2\|\mathcal{M}\|_F) \approx 0.489$  at  $n = 1000$  and  $\approx 0.491$  at  $n = 10000$ , with the sequence increasing slowly and appearing to converge to a finite limit  $G_\infty \in (0, 1/2)$ . A closed-form value for  $G_\infty$  is not established here.*

*Setup and reduction.* Each row of  $\mathbf{B}$  sums to 1, so  $D_Q(i) = 1$ , and the column degrees are  $D_K(j) = H_n - H_{j-1}$  where  $H_k = \sum_{m=1}^k 1/m$ . Hence

$$\mathcal{M}_{ij} = \frac{\mathbf{1}\{j \leq i\}}{i \sqrt{H_n - H_{j-1}}}.$$

Since  $\mathcal{M}$  is strictly lower-triangular and  $\mathcal{M}^\top$  is strictly upper-triangular,  $\|\mathcal{M} - \mathcal{M}^\top\|_F^2 = 4 \sum_{i>j} \mathcal{M}_{ij}^2$ , and

$$G(\mathcal{M})^2 = \frac{\sum_{i>j} \mathcal{M}_{ij}^2}{\|\mathcal{M}\|_F^2} = \frac{\sum_{j=1}^{n-1} S_2(j+1, n)/(H_n - H_{j-1})}{\sum_{j=1}^n S_2(j, n)/(H_n - H_{j-1})}, \quad (11)$$

where  $S_2(j, n) = \sum_{i=j}^n 1/i^2$ . The qualitative claim  $G > 0$  for all  $n \geq 2$  is immediate: at least one off-diagonal term is positive while the diagonal contribution remains finite.

*Numerical evidence.* Evaluating (11) directly:  $G(10) \approx 0.451$ ,  $G(100) \approx 0.481$ ,  $G(1000) \approx 0.489$ ,  $G(10000) \approx 0.491$ . The sequence is monotonically increasing and bounded above by  $1/2$  (since  $\mathcal{M}$  has nonzero diagonal). We record  $G_\infty < 1/2$  as a numerical observation; a closed-form value, if it exists, requires a more delicate harmonic-sum analysis that we do not pursue here. The strict inequality  $G_\infty > 0$  is all that is required for the architecture-dependent interpretation in Sec. 5.

**Lemma 29 (G for diagonal attention)** *For diagonal attention  $\mathbf{B} = I$  (pure self-focus),  $G = 0$ .*

**Proof.** When  $\mathbf{B} = I$ , we have  $D_Q = D_K = I$ , so  $\mathcal{M} = I$ . Since  $I = I^\top$ ,  $\mathcal{M}_{\text{asym}} = 0$  and hence  $G = 0$ .  $\square$

**Lemma 30 (G for symmetric bidirectional attention)** *For any symmetric attention pattern  $\mathbf{B} = \mathbf{B}^\top$  with equal row/column sums,  $G = 0$ .*

**Proof.** If  $\mathbf{B} = \mathbf{B}^\top$ , then  $D_Q = D_K$  (row sums equal column sums). Therefore  $\mathcal{M} = D_Q^{-1/2} \mathbf{B} D_K^{-1/2} = D_Q^{-1/2} \mathbf{B} D_Q^{-1/2}$ , which is symmetric:  $\mathcal{M} = \mathcal{M}^\top$ . Hence  $\mathcal{M}_{\text{asym}} = 0$  and  $G = 0$ .  $\square$

**Bimodality in decoder attention.** Real decoder heads interpolate between uniform causal ( $G \approx 0.49$ ) and diagonal ( $G = 0$ ) patterns. Heads that focus on recent tokens approach diagonal structure, yielding  $G \approx 0.1$ – $0.2$ . Heads with broad temporal attention approach uniform causal, yielding  $G \approx 0.35$ – $0.5$ . This produces the observed bimodal distribution in decoder self-attention.

**Encoder attention baseline.** Encoder attention can learn approximately symmetric patterns, yielding  $G \ll 0.1$ . When query and key representations are similar ( $q_i \approx k_i$ ), softmax attention  $A_{ij} \propto \exp(q_i^\top k_j)$  is approximately symmetric, and  $G$  approaches zero.

## C Characterization of the Asymmetry Coefficient $G$

This section characterizes the asymmetry coefficient  $G$  for diagonal, causal, and encoder versus decoder attention, establishing the foundation for using  $G$  as a temporal-isolation diagnostic.

**Theorem 31 (Diagonal attention has  $G = 0$ )** *For the diagonal attention matrix  $\mathcal{M} = I$  (pure self-attention),  $G(\mathcal{M}, \varepsilon) = 0$  for any regularization  $\varepsilon > 0$ .*

**Proof.** The diagonal matrix  $I$  is symmetric:  $I = I^\top$ . Therefore  $\mathcal{M}_{\text{asym}} = (I - I^\top)/2 = 0$ , and

$$G(I, \varepsilon) = \frac{\|\mathcal{M}_{\text{asym}}\|_F}{\|I\|_F + \varepsilon} = \frac{0}{\|I\|_F + \varepsilon} = 0.$$

$\square$

**Mechanistic interpretation.** When attention concentrates on the diagonal, each token attends only to itself, ignoring contextual history. This is the *temporal isolation* failure mode: the causal structure exists but is not exploited. Conductance may remain moderate (mass flows along the diagonal), but the model fails to integrate historical context.

**Theorem 32 (Causal attention with off-diagonal mass has  $G > 0$ )** *Let  $\mathcal{M}$  be a lower-triangular matrix ( $\mathcal{M}_{ij} = 0$  for  $j > i$ ) with off-diagonal mass (i.e.,  $\exists i, j$  with  $j < i$  and  $\mathcal{M}_{ij} \neq 0$ ). Then  $G(\mathcal{M}, 0) > 0$ .*

**Proof.** The key observation is that for  $j < i$ :

- $\mathcal{M}_{ij}$  may be non-zero (below-diagonal entry)
- $\mathcal{M}_{ji} = 0$  (above-diagonal entry, by lower-triangularity)

Therefore the antisymmetric part satisfies:

$$(\mathcal{M}_{\text{asym}})_{ij} = \frac{\mathcal{M}_{ij} - \mathcal{M}_{ji}}{2} = \frac{\mathcal{M}_{ij}}{2} \neq 0$$

for at least one pair  $(i, j)$  with  $j < i$ . This implies  $\mathcal{M}_{\text{asym}} \neq 0$ , hence  $\|\mathcal{M}_{\text{asym}}\|_F > 0$ , and therefore  $G(\mathcal{M}, 0) > 0$ .  $\square$

**Mechanistic interpretation.** Any causal attention pattern that uses historical context (attending to past tokens, not just self) necessarily has  $G > 0$ . The off-diagonal mass below the diagonal represents information flow from the past, which creates irreversible transport that  $G$  detects.

**Corollary 33 (Uniform causal attention has  $G > 0$ )** *For uniform causal attention  $\mathbf{B}_{ij} = \frac{1}{i+1} \mathbf{1}\{j \leq i\}$  with  $n \geq 2$ ,  $G(\mathcal{M}, 0) > 0$  where  $\mathcal{M}$  is the degree-normalized operator.*

**Proof.** Uniform causal attention has off-diagonal mass: entry  $(1, 0)$  equals  $1/2 \neq 0$ . By Theorem 32,  $G > 0$ .  $\square$

**Proposition 34 (Asymmetric ceiling for causal Toeplitz attention)** *Let  $\mathcal{M}$  be a causal Toeplitz matrix,  $\mathcal{M}_{ij} = f(i - j) \mathbf{1}\{j \leq i\}$  for a kernel  $f : \mathbb{N} \rightarrow \mathbb{R}$ , with  $\mathcal{M} \neq 0$ . Then  $G(\mathcal{M}, 0) \leq 1/\sqrt{2}$ , with equality if and only if the diagonal kernel vanishes ( $f(0) = 0$ ), i.e.  $\mathcal{M}$  is a strict lower-triangular causal pattern. In particular  $G = 1$  is unreachable within the causal-attention class.*

**Proof.** By the causal Toeplitz Frobenius identity, the antisymmetric energy is  $\|\mathcal{M}_{\text{asym}}\|_F^2 = \frac{1}{2} \sum_{i>j} f(i - j)^2$ . Splitting the total energy into its strict-lower-triangular part and its diagonal,

$$\|\mathcal{M}\|_F^2 = \sum_{i \geq j} f(i - j)^2 = \sum_{i > j} f(i - j)^2 + n f(0)^2.$$

Hence, writing  $S = \sum_{i > j} f(i - j)^2 > 0$ ,

$$G(\mathcal{M}, 0)^2 = \frac{\|\mathcal{M}_{\text{asym}}\|_F^2}{\|\mathcal{M}\|_F^2} = \frac{\frac{1}{2} S}{S + n f(0)^2} \leq \frac{1}{2},$$

so  $G(\mathcal{M}, 0) \leq 1/\sqrt{2}$ . Equality holds iff  $n f(0)^2 = 0$ , i.e.  $f(0) = 0$ , in which case  $G(\mathcal{M}, 0) = 1/\sqrt{2}$  exactly. The value  $G = 1$  would require  $\|\mathcal{M}_{\text{asym}}\|_F = \|\mathcal{M}\|_F$ , i.e. a purely skew operator  $\mathcal{M}^\top = -\mathcal{M}$ ; a non-negative attention matrix with any shared-support mass cannot satisfy this.  $\square$

**Mechanistic interpretation.** The strict lower-triangular pattern (every query attending only to strictly earlier tokens, never to itself) is the antisymmetric-maximal point of the causal-attention class. Its asymmetry coefficient is  $1/\sqrt{2}$ , not 1: any diagonal (self-attention) mass adds symmetric energy and pulls  $G$  strictly below the ceiling. This corrects the intuition that causal masking drives  $G$  toward its absolute maximum; the causal class is capped at  $1/\sqrt{2}$ .

**Lemma 35 (Degree normalization preserves structure)** *Degree normalization preserves the structural properties relevant to  $G$ :*

1. If  $\mathcal{M}$  is lower-triangular, then  $D_Q^{-1/2}\mathcal{M}D_K^{-1/2}$  is lower-triangular.
2. If  $\mathcal{M}$  is symmetric, then  $D^{-1/2}\mathcal{M}D^{-1/2}$  is symmetric.

**Proof. (1)** The  $(i, j)$  entry of  $D_Q^{-1/2}\mathcal{M}D_K^{-1/2}$  is  $D_Q(i)^{-1/2}\mathcal{M}_{ij}D_K(j)^{-1/2}$ . If  $j > i$ , then  $\mathcal{M}_{ij} = 0$  by lower-triangularity, so the normalized entry is also 0.

**(2)** For symmetric  $\mathcal{M}$  with  $D_Q = D_K = D$ , the normalized matrix satisfies:

$$\begin{aligned} (D^{-1/2}\mathcal{M}D^{-1/2})_{ij} &= D(i)^{-1/2}\mathcal{M}_{ij}D(j)^{-1/2} \\ &= D(j)^{-1/2}\mathcal{M}_{ji}D(i)^{-1/2} \\ &= (D^{-1/2}\mathcal{M}D^{-1/2})_{ji}. \end{aligned}$$

□

## C.1 Encoder vs. Decoder: The Critical Distinction

The theorems above establish that  $G = 0$  for *any* symmetric matrix. This creates a fundamental interpretive asymmetry between encoder and decoder attention:

- **Decoder attention:**  $G = 0$  implies diagonal concentration (temporal isolation failure)
- **Encoder attention:**  $G = 0$  is achievable with off-diagonal mass (normal operation)

The following theorems formalize this distinction.

**Theorem 36 ( $G = 0$  iff symmetric)** *For a non-zero matrix  $\mathcal{M}$ ,  $G(\mathcal{M}, 0) = 0$  if and only if  $\mathcal{M}$  is symmetric.*

**Proof. ( $\Rightarrow$ )** If  $G = 0$ , then  $\|\mathcal{M}_{\text{asym}}\|_F = 0$ , hence  $\mathcal{M}_{\text{asym}} = 0$ . From the decomposition  $\mathcal{M} = \mathcal{M}_{\text{sym}} + \mathcal{M}_{\text{asym}}$ , we have  $\mathcal{M} = \mathcal{M}_{\text{sym}}$ , so  $\mathcal{M}$  is symmetric.

**( $\Leftarrow$ )** If  $\mathcal{M} = \mathcal{M}^\top$ , then  $\mathcal{M}_{\text{asym}} = (\mathcal{M} - \mathcal{M}^\top)/2 = 0$ , hence  $G = 0$ . □

**Theorem 37 ( $G$  as distance to symmetric subspace)** *For any non-zero matrix  $\mathcal{M}$ :*

$$G(\mathcal{M}, 0) = \frac{\|\mathcal{M} - \mathcal{M}_{\text{sym}}\|_F}{\|\mathcal{M}\|_F} = \frac{d(\mathcal{M}, \mathcal{S})}{\|\mathcal{M}\|_F},$$

where  $\mathcal{S}$  is the subspace of symmetric matrices and  $d(\mathcal{M}, \mathcal{S})$  is the Frobenius distance.

**Proof.** By orthogonality of  $\mathcal{M}_{\text{sym}}$  and  $\mathcal{M}_{\text{asym}}$ , the closest symmetric matrix to  $\mathcal{M}$  is  $\mathcal{M}_{\text{sym}}$ . Therefore  $d(\mathcal{M}, \mathcal{S}) = \|\mathcal{M} - \mathcal{M}_{\text{sym}}\| = \|\mathcal{M}_{\text{asym}}\|_F$ , and the result follows from the definition of  $G$ . □

**Theorem 38 (Blindness is trivial for symmetric matrices)** *When  $\mathcal{M}$  is symmetric, the orientation blindness theorem (Theorem 5) is trivially satisfied:  $\mathcal{H}(\mathcal{M}) = \mathcal{H}(\mathcal{M}^\top)$  directly because  $\mathcal{M} = \mathcal{M}^\top$ .*

**Proof.** If  $\mathcal{M} = \mathcal{M}^\top$ , then  $\mathcal{H}(\mathcal{M}) = \mathcal{H}(\mathcal{M}^\top)$  by substitution. □

**Mechanistic interpretation.** When  $\mathcal{M}$  is symmetric, the orientation blindness theorem provides no information loss: the dilation is identical under transpose because the matrix itself is identical under transpose. This is the *trivial case* where blindness is vacuous.

**Theorem 39 (Encoder admits  $G = 0$  with off-diagonal mass)** *For  $n \geq 2$ , there exists a non-zero symmetric matrix  $\mathcal{M}$  that is not lower-triangular (i.e., not causal) and has off-diagonal entries. Such matrices satisfy  $G(\mathcal{M}, 0) = 0$  despite having substantial off-diagonal structure.*

**Proof.** Construct  $\mathcal{M}$  with  $\mathcal{M}_{ii} = 1$ ,  $\mathcal{M}_{i,i+1} = \mathcal{M}_{i+1,i} = 1/2$ , and zeros elsewhere. This matrix is symmetric (hence  $G = 0$ ), non-zero, and has  $\mathcal{M}_{01} = 1/2 \neq 0$  (an above-diagonal entry, so not causal).  $\square$

**Corollary 40 (Encoder–decoder  $G$  distinction)** *The diagnostic interpretation of  $G = 0$  differs fundamentally by attention type:*

1. **Decoder (causal):** *If  $\mathcal{M}$  is causal and  $\mathcal{M} \neq 0$  and  $G(\mathcal{M}, 0) = 0$ , then  $\mathcal{M}$  has no off-diagonal mass below the diagonal; i.e.,  $\mathcal{M}$  is diagonal (temporal isolation failure).*
2. **Encoder (non-causal):**  *$G = 0$  is achievable with off-diagonal mass via symmetric patterns, representing normal bidirectional attention.*

**Proof. (1)** By Theorem 36,  $G = 0$  implies  $\mathcal{M}$  is symmetric. A causal matrix  $\mathcal{M}$  with  $\mathcal{M}_{ij} = 0$  for  $j > i$  that is also symmetric must have  $\mathcal{M}_{ij} = \mathcal{M}_{ji} = 0$  for all  $i \neq j$ . Thus  $\mathcal{M}$  is diagonal.

**(2)** Theorem 39 provides the explicit construction.  $\square$

**Summary of diagnostic logic.** The formal results establish a clear diagnostic framework with *attention-type-specific interpretation*:

Attention	Pattern	$G$	Interpretation
Decoder	Diagonal	0	Temporal isolation
Decoder	Causal + history	$>0$	Using context
Encoder	Symmetric	0	Normal
Encoder	Asymmetric	$>0$	Directional bias

Thus  $G$  provides a mechanistic signal for temporal isolation *specifically in decoder self-attention*. For encoder attention,  $G = 0$  is the expected baseline for symmetric routing patterns, and  $G > 0$  indicates asymmetric directional bias that may warrant investigation. This distinction is critical for correct interpretation across encoder-decoder architectures.